The Astrophysical Journal, 911:129 (20pp), 2021 April 20 https://doi.org/10.3847/1538-4357/abe7f3

Energy Deposition by Cosmic Rays in the Molecular Cloud Using GEANT4 Code and Voyager I Data

Mauricio Tizziani Pazianotto[1], Sergio Pilling[2], Jose Manuel Quesada Molina[3], and Claudio Antonio Federico[4]
[1] Instituto Tecnológico de Aeronáutica, S. J. dos Campos, Brazil
[2] Universidade do Vale do Paraíba, S. J. dos Campos, Brazil
[3] University of Seville, Seville, Spain
[4] Institute for Advanced Studies, S. J. dos Campos, Brazil
Received 2020 December 21; revised 2021 February 12; accepted 2021 February 14; published 2021 April 26

Abstract

Molecular clouds (MCs) are exposed to Galactic and extragalactic cosmic rays (CR) that trigger several physical and physicochemical changes, including gas and grain heating and molecular destruction and formation. Here we present a theoretical model describing the energy delivered by CRs, composed of protons, alphas, and electrons taken from Voyager I measurements, into a typical MC with 5400 $M_{\odot}$ (composed mainly of H with a density law of $r^{-1.2}$) and size around 1×10^6 au. The calculation was performed employing the Monte Carlo toolkit GEANT4 to obtain the energy deposition per mass from several types of secondary particles (considering nuclear and hadron physics). The results indicate that incoming protons contribute to most of the energy delivered in the MC in all regions (maximum $\sim$230 MeV g^{-1} s^{-1} at outer regions of the cloud). Secondary electrons are the second most important component for energy deposition in almost all layers of the MC and can deliver an energy rate of $\sim$130 MeV g^{-1} s^{-1} in the outer region of the MC. Other cascade particles have their major energy delivery in the central and denser core of the MC. From a temperature model (considering CR data from Voyager I), we observed (i) a small bump in temperature at the distance of 3×10^3–2×10^4 au from the center, (ii) a rapid temperature decrease (roughly 7 K) between the outer layer and the second most outer layer, and (iii) that, at a distance of 5×10^4 au ($Av > 10$), the gas temperature of the MC is below 15 K.

Unified Astronomy Thesaurus concepts: Molecular clouds (1072); Cosmic ray showers (327); Secondary cosmic rays (1438)

1. Introduction

As pointed out by Goldsmith & Langer (1978) and Galli & Padovani (2015), cosmic rays (CRs) are an efficient (often dominant) source of heating in various environments in the interstellar medium (ISM), in particular in dense molecular cloud (MC) cores shielded from the external ultraviolet radiation field (with visual extinctions $A_V > \sim 5$). In such dense and obscured clouds, the incoming Galactic and extragalactic CR delivers its energy in several processes, the ionization of molecular hydrogen gas being the most studied and dominant one. In such processes, the free electron's energy depends only weakly on the CR's energy and is typically $\sim$30 eV. Following the ionization, the electron cannot easily transfer its energy to other particles in the gas directly, because its tiny mass guarantees that most collisions are elastic and transfer no energy to the impacted particle. However, the electron also has enough energy to ionize, dissociate, and/or heat other hydrogen molecules. Secondary ionizations do indeed occur, but in this case, almost all the energy goes into ionizing the molecule ($\sim$15 eV), and the resulting electron has the same problem as the first one. Summing over all possible transfer channels and including heating by secondary ionizations, the energy yield per primary CR ionization is in the range 7–20 eV, depending on the density (Glassgold & Langer 1973; Dalgarno et al. 1999). As pointed out by Wolfire et al. (2010), combining this energy yield with the primary CR ionization rate (CRIR) in the Milky Way, which is observationally estimated to be about 2×10^{-17} s^{-1} per H nucleus, it is possible to obtain the total heating rate per H atom of CR (G_{CR}) $\sim 1 \times 10^{-27}$ erg s^{-1} $\sim 6 \times 10^{-16}$ eV s^{-1} $\sim 2 \times 10^{-8}$ eV yr^{-1}. Finally, considering the mass of hydrogen and its abundance as the dominant species, the power delivered by CRs per nanogram of material in the dense clouds is roughly 0.4 eV ng^{-1} s^{-1}.

The irradiation of MCs by CRs triggers several physical and physicochemical changes that range from energy delivery that heats up the system and particle formation (intranuclear cascade) to molecular destruction and eventually formation of new species (e.g., Dalgarno 2006; Padovani et al. 2009). All of the particles produced during the interaction (i.e., protons, neutrons, muons, pions, electrons, photons, etc.) interact with the medium by different processes depositing their energy directly and indirectly. A great effort has been made to understand the energy deposition at different regions in the MC for different CR-induced particles, as well as its contribution to the heat balance in the cloud. The cooling processes of such clouds are ruled by two main mechanisms, as noted by Krumholz (2011): molecular lines (mostly CO excited by inelastic collision with hydrogen atoms following line emission at the IR and radio wavelengths) and dust radiation (thermal emission in the IR and radio wavelengths). However, dust is only able to cool the gas if collisions between dust grains and hydrogen molecules occur often enough to keep them thermally well coupled, which should occur at number densities around 10^4 cm^{-3} (Goldsmith 2001); otherwise, the grains cool off, but the gas stays hot. Since this density is higher than the typical density in an MC (except in the very central regions) in the outer layers, the gas and dust might have different temperatures.

The interactions between CRs with space environments such as MCs and protoplanetary disks by employing Monte Carlo simulations have been performed in the literature by several

groups (e.g., Wood et al. 2004; Herbst & Cuppen 2005; Padovani et al. 2009; Boettcher et al. 2013; Padovani & Galli 2013; Vaupre 2015; Cui et al. 2016; Kataoka & Sato 2017; Vandenbroucke & Wood 2018; Vandenbroucke et al. 2018). In these models, the authors often observed that the heating produced by CRs sometimes explains observational features (e.g., emission lines, infrared emission, desorption of molecules from grains) and sometimes does not (e.g., some forbidden lines, energy profile within the clouds). Besides, for the study of the ISM, Monte Carlo simulations of CRs have also been performed to understand the energy processing induced by CRs in other astrophysical environments, as shown by Helling et al. (2016), who studied the effect of CRs by triggering ionization and discharge processes in the atmospheres of brown dwarfs and extrasolar planets. It is worth noting that most of these models consider the energy input due to CRs as coming exclusively from protons or proton+alpha particles, often simply ruled by the interaction cross section (e.g., see also Padovani & Galli 2013). The cascade particles (and the energies involved in the production and release of secondary particles) are not taken into consideration in most of these models. In the current work, we attempt to clarify the energy delivered by cascade particles and the secondary particle distribution within a selected astrophysical environment, an MC with a size of roughly 1×10^6 au (~15.9 lt-yr ~ 4.8 pc) and mass around 5400 $M_\odot$.

In the current work, we compute the energy delivery by CRs in MCs not considering the canonical value of the CRIR determined mainly from the collision cross section between fast protons with hydrogen atoms (e.g., Yeghikyan 2011) but considering the energy delivered by the CR inventory taken from measurements from the Voyager I spacecraft at the ISM (Cummings et al. 2016). The primary sources consider protons, alphas, and electrons with energies up to 1 TeV and their cascade particles during collision with matter. The calculation was performed employing a Monte Carlo–based code (GEANT4; Agostinelli et al. 2003; Allison et al. 2006) and obtained the energy deposition per mass for several types of particles (with the particle cascade) along the MC, as well as its energy distribution within the cloud. All reactions, the nuclear data library, and the scattering process for several types of particles were considered as possible. The importance of determining the energy deposition is that it can be used to estimate the heating or temperature profile of the medium. Since the temperature influences chemical reactions, the incoming CRs, as well as their secondary particles, also affect the chemical balance of the medium. Therefore, besides the direct processing (collisions target atoms and molecules), the energy input of CRs and secondary particle ions, written in terms of temperature, also has implications in the astrochemistry and astrobiology fields. In the current paper, we present a first-order approximation model to compute such a temperature-induced profile inside the MC considering the simple heating (with a parameter to handle its efficiency) due to the incoming CRs. Future models can handle this issue in a more proper way.

In Section 2, we present the theoretical and computational methodologies employed in this work using by the GEANT4 code, following the cascade processes of nuclear physics and geometry and model parameters employed in this study. The main results and discussion are given in Section 3, with an emphasis on the energy delivered by each particle in the cascade particle inventory during collisions inside the cloud. Section 3 also presents additional subsections with a first-order model for the temperature enhancement inside the MC due to energy delivered by CRs and a comparison with a model employing a CR flux modulated by solar potential (with a cut for low-energy ions). Some astrophysical implications are also provided. A summary and conclusions are presented in Section 4.

2. Methodology

We have modeled the MC geometry, composition, and cosmic radiation transport using the Monte Carlo toolkit GEANT4 v10.1 (Agostinelli et al. 2003; Allison et al. 2006). The following topics present the main aspects of the simulations performed in the present work: the modeling of the MC geometry and composition, the generation of the incident cosmic radiation, and the GEANT4 physics considered.

Initially, the code MCNPX v2.5 (Pelowitz 2005) was used for the simulations, but it proved unsuitable for the task due to the huge dimensions of the geometry and the very low density of the materials involved. The results suggested that the MCNPX neglects the neutron decay that is a very important effect of this kind of environment of simulation. Therefore, all results and simulations in this work were obtained by GEANT4 simulations.

2.1. Geometry and Composition Modeling

In order to model the MC's geometry, we have considered a sphere divided into 13 spherical layers with different radii, where the density varies as $r^{-1.2}$, with r being the mean radius of each layer. The value of the power-law index -1.2 was considered as an average index for the density distribution profile of MCs (see also Toci & Galli 2015). The total mass of the MC considered in the current model was about 5400 $M_\odot$ (value within the range of masses of the observed MCs; Roman-Duval et al. 2010).

The composition of the modeled MC corresponds to a mixture of H_2 and carbonaceous grains (expressed in terms of H and C atoms). We have considered grains with a density of 2.1 g cm^{-3} and a radius of 50 nm. In this way, each layer is composed of 99.83% H_2 (H+H atoms) and 0.17% C atoms (dust/gas mass ratio of 1/100). The ratio of dust to gas mass in the Milky Way has long been established to be around 1:100 in the diffuse ISM (e.g., Bohlin et al. 1978), with sizes typically below 1 μm in MCs (Tricco et al. 2017). Table 1 shows the radii, densities, and masses considered for each MC layer.

In our model, the carbon atoms (described within the canonical dust/gas mass ratio of 1/100; Draine 2003) are the typical representant for the astrophysical dust (carbonaceous-rich grains). As noted by several authors, such as Tielens & Allamandola (1987), Jessberger et al. (2001), Draine (2003), and Flynn et al. (2016), the carbon atom is by far one of the most abundant species of dust grains in space, followed by other elements such as Cr, Ca, Al, Mg, Na, Si, O, and Fe. Additionally, depending on the local temperature and shielding within the cloud, the dust grains might also have a small cap containing water-rich ice. Future simulations may take into account other atomic species besides carbon atoms to describe the dust phase in an attempt to identify the effects of minor components (including O, Si, Fe, and other refractory and low

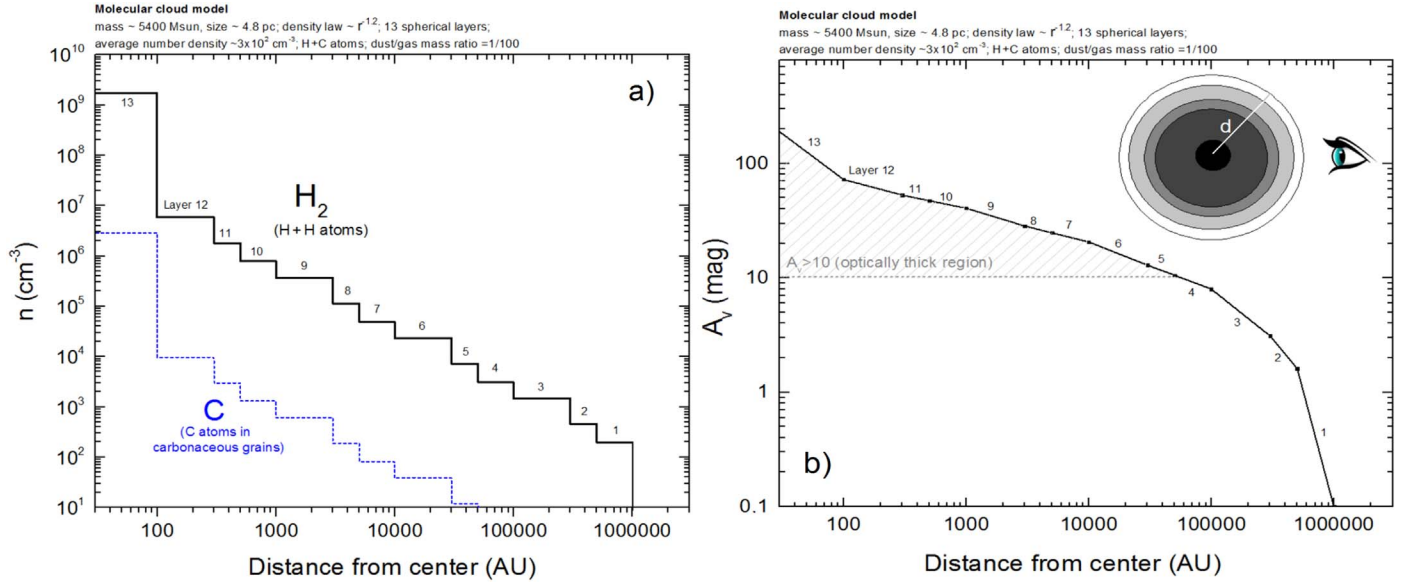

Figure 1. Number density profile (panel (a)) and average visual extinction profile (panel (b)) of each layer as a function of distance from the center for the employed MC model. See details in the text.

Table 1
Properties of the Spherical Layers Employed in the Modeling

Layer No.	Outer and Inner Radii (au)	Outer and Inner Radii (km)	Density (g cm^{-3})	Mass (g)
1	9.4E+05–5.0E+05	1.4E+14–7.5E+13	6.5E−22	6.8E+36
2	5.0E+05–3.0E+05	7.5E+13–4.5E+13	1.5E−21	2.1E+36
3	3.0E+05–1.0E+05	4.5E+13–1.5E+13	4.8E−21	1.8E+36
4[a]	1.0E+05–5.0E+04	1.5E+13–7.5E+12	1.0E−20	1.3E+35
5	5.0E+04–3.0E+04	7.5E+12–4.5E+12	2.4E−20	3.3E+34
6	3.0E+04–1.0E+04	4.5E+12–1.5E+12	7.7E−20	2.8E+34
7	1.0E+04–5.0E+03	1.5E+12–7.5E+11	1.6E−19	2.0E+33
8	5000–3000	7.5E+11–4.5E+11	3.7E−19	5.2E+32
9[b]	3000–1000	4.5E+11–1.5E+11	1.2E−18	4.5E+32
10	1000–500	1.5E+11–7.5E+10	2.6E−18	3.2E+31
11	500–300	7.5E+10–4.5E+10	5.9E−18	8.2E+30
12	300–100	4.5E+10–1.5E+10	1.9E−17	7.0E+30
13[c]	100–0	1.5E+10−0	5.7E−15	8.0E+31
			Total	1.08E+37[d]

Notes.
[a] Outer boundary of Oort cloud.
[b] Inner boundary of Oort cloud.
[c] Heliopause and outer boundary of trans-Neptunian objects.
[d] 1.08×10^{37} g $\sim$ 5400 $M_{\odot}$.

abundant heavy atoms) and also the ice cap on the grains in the energy deposition by CRs within interstellar clouds.

Figure 1 presents the number density profile (panel (a)) and the visual extinction profile (panel (b)) for the employed MC model. The visual extinction (Av) was calculated considering the line of sight looking direct toward the object and the canonical relation, $Av\ (\mathrm{mag}) = N_{\mathrm{H}}/1.8 \times 10^{21}\ \mathrm{cm}^{-2}$, where we considered the column density of hydrogen to be the double of hydrogen molecules ($N_{\mathrm{H}} = N_{\mathrm{H2}}{}^{*}\ 2$). For each layer, the N_{H2} is calculated by considering the number density (n_{H2}) times the layer thickness. From panel (b), we observe that for the current model with 5400 $M_{\odot}$, the visual extinction reaches values above 10 mag (optically thick region) for a radius below 10^5 au. Therefore, regions below 10^5 au are very shielded from the external UV and X-rays, and the incoming energy (heating source) is only due to penetrating CRs. Indeed, as discussed by Tielens (2005) and Goldsmith (2001), CRs are most important for heating in dark regions of interstellar clouds.

2.2. Cosmic Radiation Modeling

The cosmic radiation incident into the MC was modeled by considering the spectra of the primary cosmic radiation, as well as the angle of incidence, in order to reproduce the isotropic radiation field. The following subsections will describe both aspects.

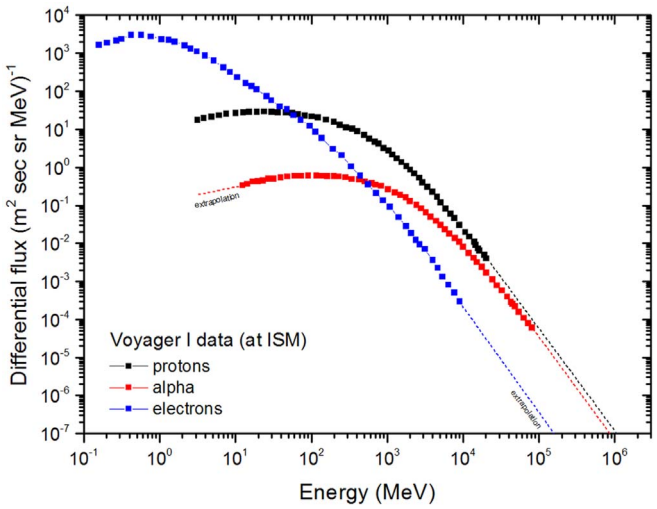

Figure 2. Primary CR spectra considered in the simulations obtained from measurements of the Voyager I spacecraft outside the solar system (taken from Cummings et al. 2016). Dashed lines are extrapolations to complete the data set.

2.2.1. Particle Spectra

The primary cosmic radiation considered in the simulations was based on the data measured by the Voyager I spacecraft outside the limits of the solar system (Cummings et al. 2016). From the Voyager data, we select the proton, alpha, and electron measurements to constitute the primary sources of CRs employed in the current model. Therefore, the primary fluence rates that we have obtained for the simulations are 1.26 protons cm^{-2} s^{-1} sr^{-1}, 0.09 alphas cm^{-2} s^{-1} sr^{-1}, and 1.19 electrons cm^{-2} s^{-1} sr^{-1}, with mean energies of 1.09 GeV, 3.45 GeV, and 45.8 MeV, respectively. Figure 2 shows the proton, alpha, and electron spectra used in the simulations (taken from Cummings et al. 2016). From this figure, we observe that low-energy electrons are the major components, in number, of the primary CR source.

2.2.2. Incidence Direction

The primary cosmic radiation incident into the MC was modeled by considering an isotropic radiation field constant in time taken from Cummings et al. (2016), and its representation in terms of source and angular distribution is presented in Figure 3. In order to reproduce the isotropic radiation field in free space, we used a spherical source in which each point is isotropically distributed on the spherical surface and emits primary particles following the cosine-law angular emission.

If the particle emission is limited by the θ angle, a detector located in the center region (i.e., a detector represented by the smallest sphere represented in Figure 3) will count a higher quantity (i.e., energy deposited) the smaller the θ. Neglecting the interactions and materials that compose the given geometry, the ratio between the number of particles impinging on a detector centered inside the spherical volume of the MC, considering a source on its surface emitting particles with angles $0 \leqslant \theta \leqslant \theta_f$ and $0 \leqslant \varphi \leqslant 360°$, and the number of particles emitted with angles $0 \leqslant \theta \leqslant 180°$ and $0 \leqslant \varphi \leqslant 360°$ (4π spheroradians), where φ is an azimuthal angle in spherical

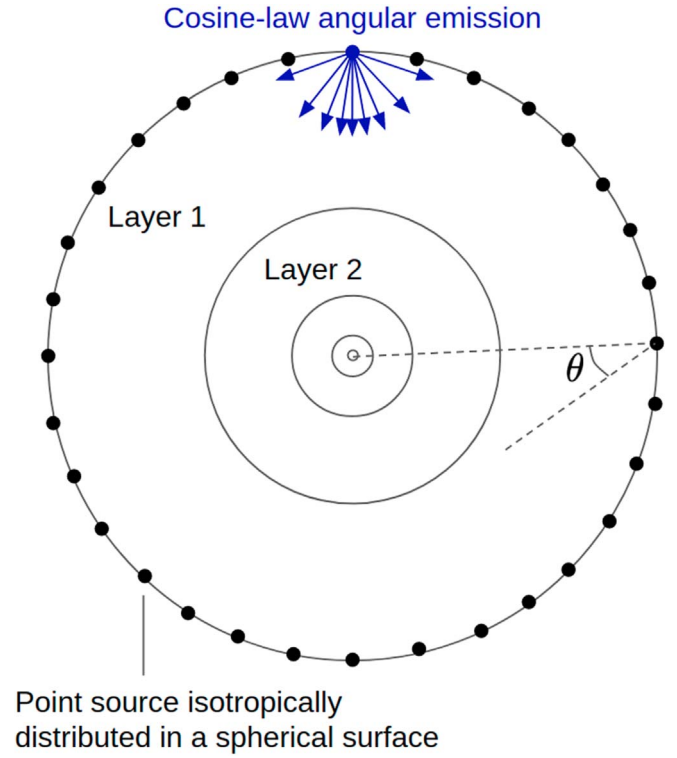

Figure 3. Source particle distribution on a spherical surface and the cosine-law angular emission representation.

coordinates, is given by

$$R_{\theta_f,180^\circ} = \int_0^{\theta_f} \cos(\theta)\sin(\theta)d\theta = \frac{\text{count}^{\theta_f}}{\text{count}^{180^\circ}}, \quad (1)$$

where count^{180° is the counting obtained due to a source with 4π spheroradian emission and count_f^{θ} is the counting obtained due to a source emitting particles with polar angles in the range $0 \leqslant \theta \leqslant \theta_f$. If we have a very small particle detector located in the central region, an emission with polar angles up to 1° will result in a counting about 6566 times higher as compared to an emission with polar angles up to 180°.

For each layer shown in Table 1, we determined the energy deposited by the different components (proton, alpha, electron, photon, electron, positron, pion+, pion−, muon+, muon−, deuteron, and triton) per mass of the respective layer as a function of primary particle type (proton and alpha). The energy deposition counting depends on the interaction between the different particles and the atoms that compose each layer. Then, due to the size of the inner layers, the energy deposition can be an extremely rare event if we consider a 4π emission, and the simulation would be too long to get results with an uncertainty lower than 10%.

Secondary neutrons and neutral pions were also analyzed, but they did not present direct energy deposition in any layer. Due to the very low density environment and huge geometry involved, these particles decay before any interaction takes place, producing protons and electrons (from the beta decay of neutrons) and gammas (from neutral pions), which deliver energy in the MC.

In order to get a relative error lower than 10% for the different particles at the inner layers, we have performed simulations with a closer solid angle emission. We have used

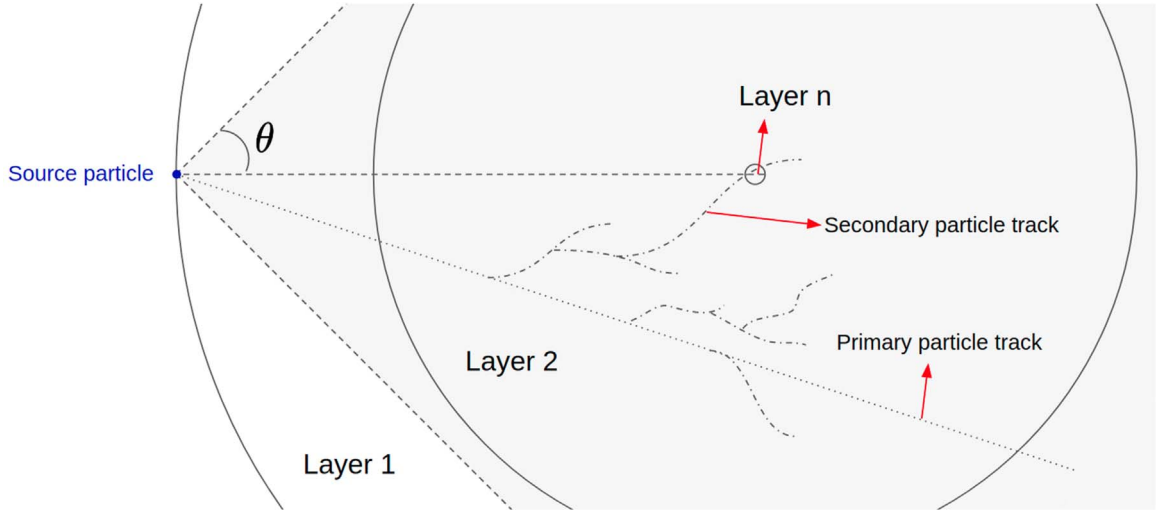

Figure 4. Representation of primary and secondary particle propagation due to the source particle emission with angle θ. Secondary particles produced at different positions could deposit energy at the inner layers.

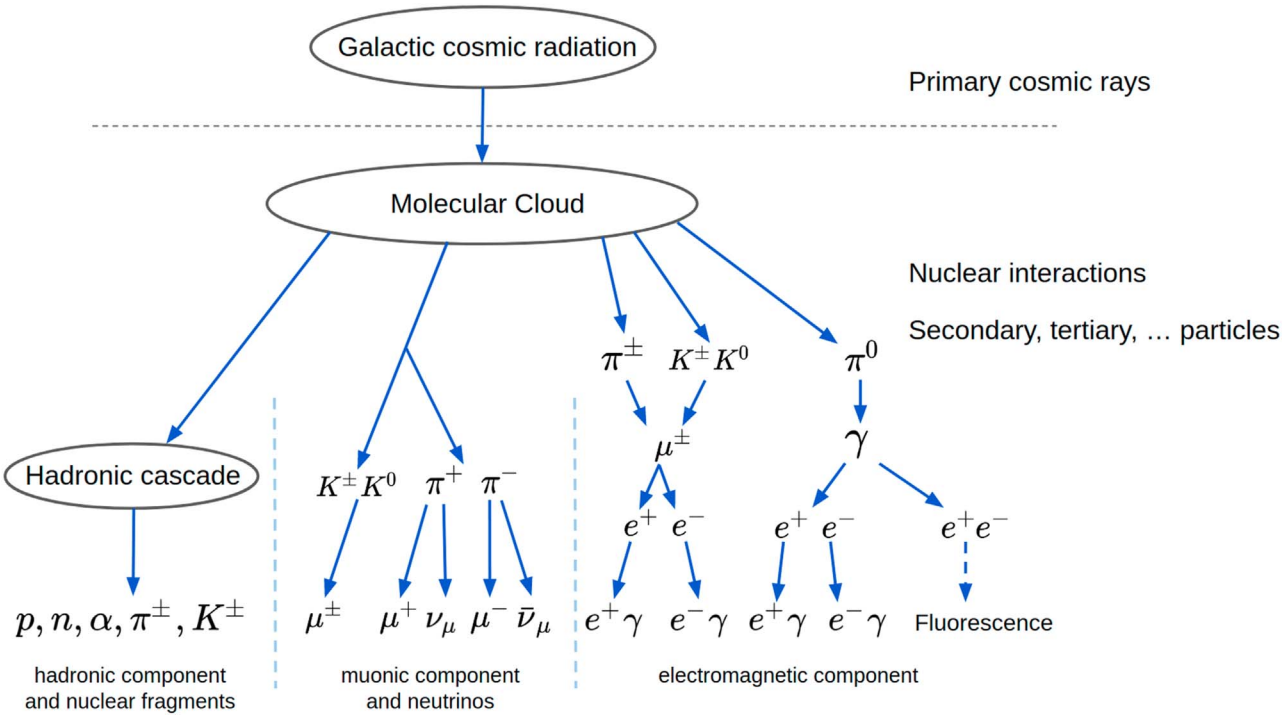

Figure 5. Schematic diagram of the CR-induced particles produced in the MC (gas phase H_2 + solid phase C grains; adapted from Filges & Goldenbaum 2010).

the following θ angles for each particle source type: 90°, 60°, 30°, 10°, 5°, 2.5°, and 1°. The higher the emission angle (θ), the more realistic the simulations are, because a secondary particle produced in regions outside the solid angle of the primary particle emission could deposit energy in the layers covered by the primary particle radiation field, as we can see in Figure 4. When we close the solid angle of emission, we are neglecting the secondary particle contribution to the energy deposited at the inner layers. From the results obtained, we selected for each layer the lowest cutoff of the emission angle providing enough statistics. For the analyses, these cutoffs in emission polar angles were much larger than the limiting polar angle corresponding to the layer of interest ($\gtrsim$3 orders of magnitude). For instance, the θ angle correspondent to the radius of the innermost layer is 5.71×10^{-3}°, which is much smaller than the cutoff angle of emission θ (1°).

This procedure is a first-order approximation. However, this is a physically sound assumption since, considering the fact that the primary radiation field is composed of high-energy particles and the very low densities involved, the mean free path of the primary particles is large. and the secondary particles are mostly produced with very close angles.

2.3. GEANT4 Parameterizations

As previously stated, all simulations of the cosmic radiation transport and interaction within the MC were performed using

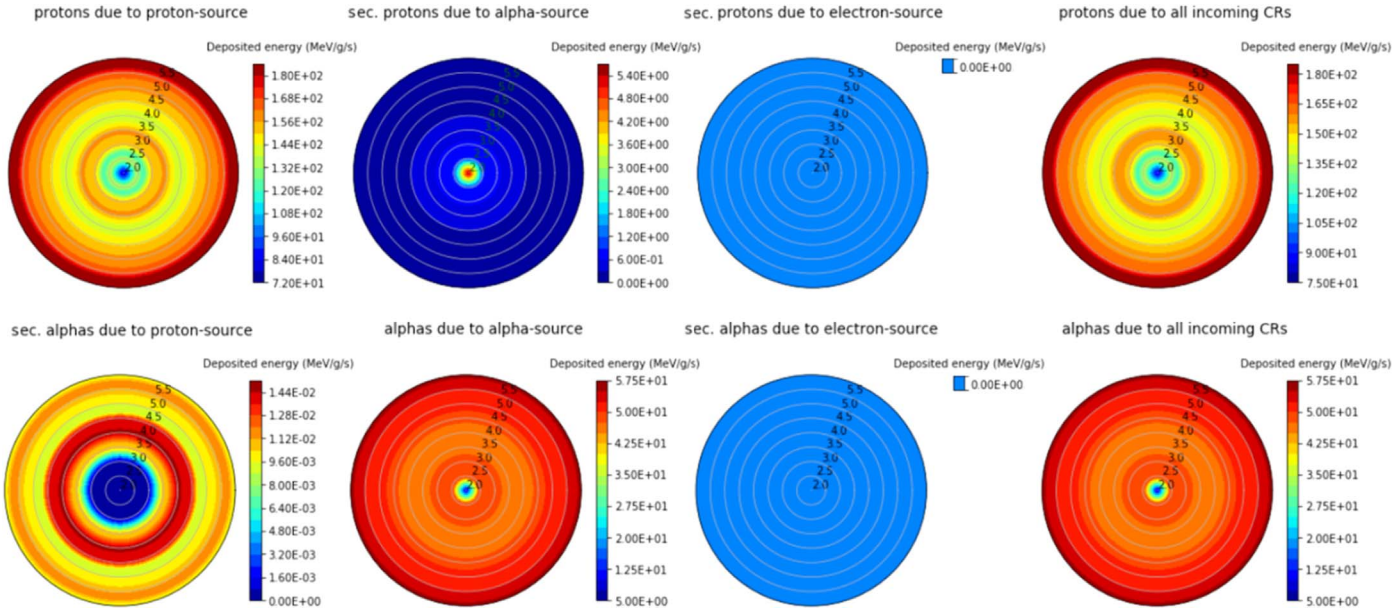

Figure 6. Color map of the energy delivery by secondary protons and alphas due to incoming CRs inside the MC. The rightmost panels present the summed values (considering proton, alpha, and electron CRs). The numbers in the radial axis are the sizes of a given outer layer in astronomical units (logarithmic scale).

the GEANT4 toolkit. Figure 5 shows a representative diagram of the main particles produced by the interaction of the CRs with the MC.

In order to simulate the hadron interactions, the simulations were carried out with the QGSP_INCLXX_HP reference physics list. The QGSP package includes the quark gluon string model for interactions of nucleons and pions for energies higher than ∼15 GeV, followed by pre-equilibrium de-excitation of the remnant fragments and the completely redesigned Liège intra-nuclear cascade model (INCL++) for lower incident energies. The _HP suffix refers to the high-precision NeutronHP package (cross section and model), which is used at energies below 20 MeV to simulate neutron elastic and inelastic scattering by means of the evaluated ENDF/B-VII.1 data library. The electromagnetic interactions of charged particles, gammas, and optical photons are simulated using G4EmStandardPhysics, which is recommended for high-energy applications (Geant4 Collaboration 2012).

The number of events considered in the simulations was 1×10^8 for each source particle (protons, alphas, and electrons) and angle of emission, totaling 35 simulations (all models) and about 300 hr on a typical 20-core computer.

3. Results and Discussions

The results are presented in the following subsections. In Section 3.1, we present the calculated deposited energy in the MC for many components due to different primary particle spectra measured by Voyager I. Section 3.2 presents calculations for the temperature in each layer of the simulated MC in a steady-state situation and including balance heat employing the current data of energy deposition and the methodology described by Goldsmith (2001).

3.1. Energy Delivered by CRs

Figure 6 shows the energy deposited in units of MeV g^{-1} s^{-1} of protons and alphas inside the MC due to incoming CR flux (protons, alphas, and electrons up to 1 TeV) considering the measurements obtained by the Voyager 1 spacecraft (Cummings et al. 2016). The upper panels indicate that the energy delivered in the outer regions of the MC comes mainly from protons with values that can reach up to ∼180 MeV g^{-1} s^{-1} (∼0.18 eV ng^{-1} s^{-1}). The second most important ionizing agents are the electrons produced by proton sources, as we will see later on. The maximum energy deposited by secondary protons due to alpha sources (∼5 MeV g^{-1} s^{-1}) occurs in the very deep regions (<100 au), in contrast with the maximum energy deposited by protons from proton sources (∼180 MeV g^{-1} s^{-1}) that is located in an external layer at around 5×10^5 au. Such a situation of maximum energy delivered in an external layer region can be explained as due to the high attenuation of protons with low energy, which are the main component of the primary proton spectrum. Since the energy transfer to matter is high for lower-energy protons, these protons will deposit their energy mostly after their passage through the first layers.

The lower panels in Figure 6 indicate that the outer part of the MC is mainly heated by protons. We observe that at the central region, the energy delivered by alphas reaches a minimum value of ∼5.50 MeV g^{-1} s^{-1} (∼5.50×10^{-3} eV ng^{-1} s^{-1}); meanwhile, in the outer regions, the energy delivered by protons is about 3 times higher than the energy delivered by alpha particles. Secondary alphas due to proton sources deliver more energy in a shell-like region between ∼1×10^3 and 3×10^4 au. The energy deposited presents values up to ∼1.40×10^{-2} MeV g^{-1} s^{-1} and decreases significantly in the center region. Models also indicate that at distances around 2000 au, the energy deposition of secondary proton emission increases.

The radial profiles of the energy deposition suggest that the main component of the proton contribution arises from the primary protons (which lose energy mainly by ionization), and, analogously, the main component of the energy deposition by alphas comes from primary alphas, which also lose their energy mainly by ionization. Secondary protons from primary protons (and alphas from primary alphas) are produced via nuclear reactions (spallation) and are less abundant. Protons from alpha primaries are secondaries from nuclear reactions (hence also

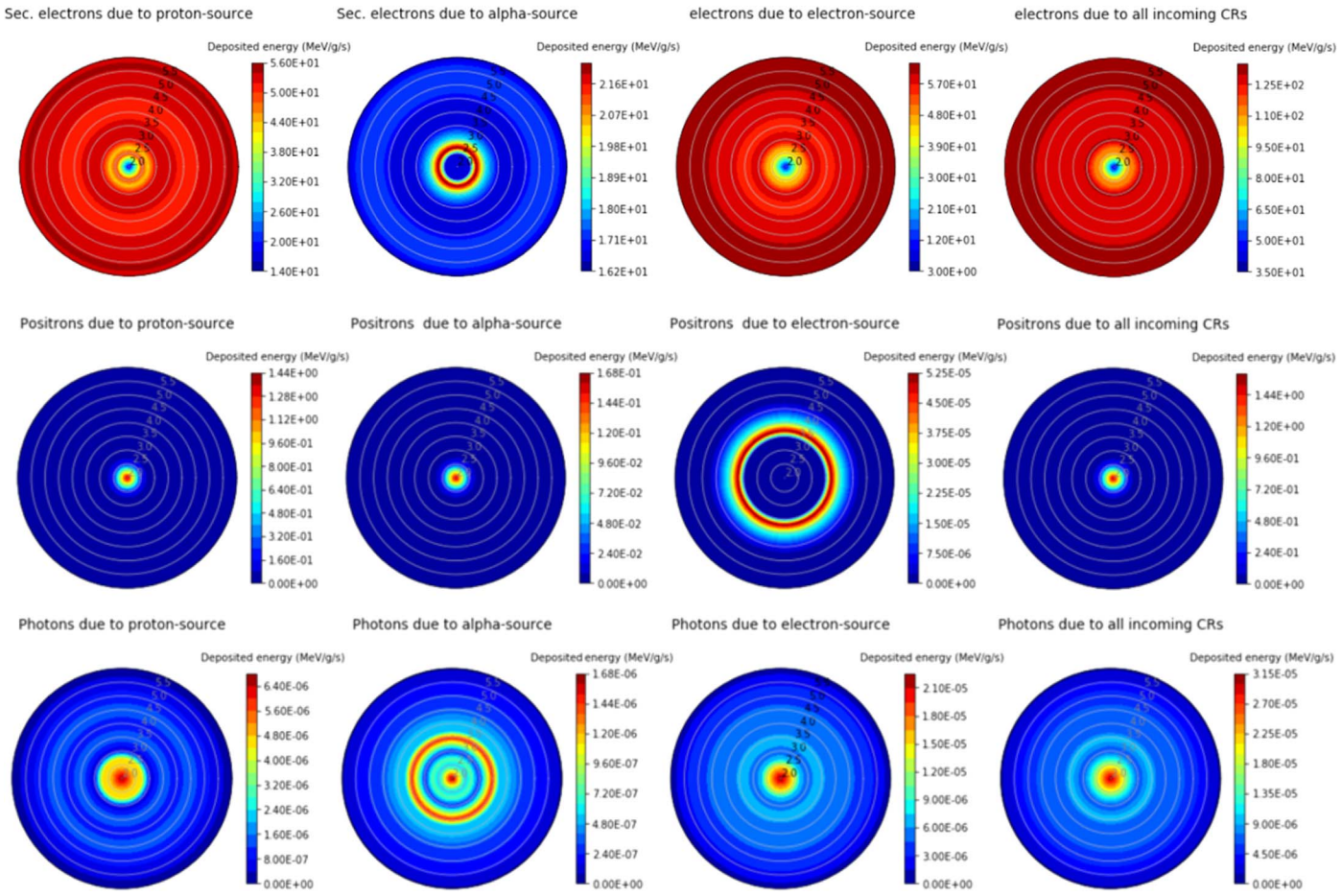

Figure 7. Color map of the energy delivery by secondary electrons, positrons, and photons (mainly gamma) due to incoming CRs inside the MC. The rightmost panels present the summed values (considering proton, alpha, and electron CRs). The numbers in the radial axis are the sizes of a given outer layer in astronomical units (logarithmic scale).

less abundant than primary protons and, accordingly, with a much smaller energy deposition) or ionization of hydrogen atoms. Both processes are favored in the inner shells of the MC, where the density is higher and the alpha particles have been stopped to the point at which their reaction cross section and ionizing capability increase at such low energies, producing secondary protons from nuclear reactions on carbon ions or ionization of hydrogen atoms. Secondary alphas from primary protons (as well as from primary alphas) arise from nuclear breakup reactions on carbon nuclei, which are governed by the reaction cross section and the channel-specific mechanism.

The primary electrons trigger the electromagnetic showers in which secondary electrons, positrons, and photons are produced. The main contribution to the energy deposition comes from the electrons, as can be seen in Figure 7, which shows the color map of the energy delivered in units of MeV g^{-1} s^{-1} by electrons (primary and secondary) and secondary positrons and photons (mainly gamma rays, X-rays, and UV) produced due to the incoming CRs (protons, alphas, and electrons up to 1 TeV) inside the MC. From this figure, we observe that most of the energy deposited is due to electrons from the primary electron and proton sources, and it presents an almost homogeneous energy deposition throughout the MC, but it presents a sudden decrease in the center region. The energy deposited reaches ∼130 MeV g^{-1} s^{-1} (∼0.13 eV ng^{-1} s^{-1}) and represents the most important component for energy deposition after the proton source. We observe in the case of the secondary positrons due to electron sources that the energy deposited presents a shell-like behavior with maximum energy deposited at around 4000 au, but this is well below the energy deposition by protons, alphas, and electrons.

The energy deposition produced by photons seems to increase as the cloud density increases (toward the center). However, as we observe in the bottom part of Figure 7, the photon energy distribution is different for each primary CR source (e.g., concentrated in the core of a cloud in the case of proton and electron sources and with a shell-like structure around 2000 au in the case of an alpha source). The characterization of the photon spectrum (e.g., the energies at the X-ray, UV, and VIS-IR ranges) produced inside MCs due to the incoming CRs will be presented in a future work.

The energy delivered by secondary deuterons and tritons produced due to the incoming CRs (protons, alphas, and electrons) inside the MC is presented in Figure 8. The upper panels indicate the energy delivered by deuterons (with energies mostly from ∼0.15 to 1.3 MeV g^{-1} s^{-1}), and the lower panels show the calculation for tritons. In the bottom part of Figure 8, we observe that secondary tritons due to primary protons deliver more energy (up to 7.2×10^{-4} MeV g^{-1} s^{-1}) in extended shell-like regions ranging from roughly 3000 to 50,000 au. The secondary tritons due to the alpha source deliver their maximum energy (∼0.14 MeV g^{-1} s^{-1}) in the very central region (<100 au). Comparing both deuteron and triton contributions, the results show that the energy deposition by deuterons in the central region

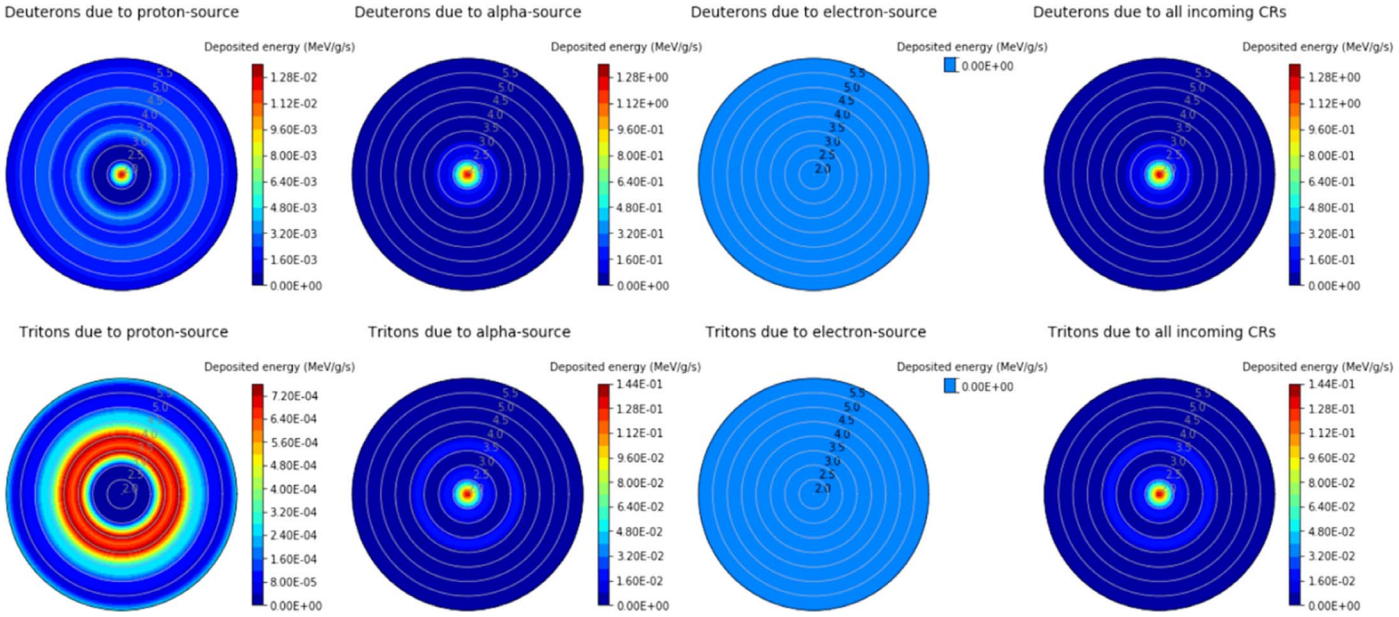

Figure 8. Color map of the energy delivery by deuterons and tritons due to incoming CRs inside the MC. The rightmost panels present the summed values (considering proton, alpha, and electron CRs). The numbers in the radial axis are the sizes of a given outer layer in astronomical units (logarithmic scale).

is about 1 order of magnitude higher than the one from tritons (considering both protons and alpha primary particles). As would be expected, most of the energy deposited by deuterons and tritons within the MC comes from the breakup of the primary alphas (alpha source) being much smaller than the one arising from primary protons, and there is no contribution of the electron source in this case.

According to the physics behind the Bragg peak (Brown & Suit 2004), the maximum energy deposition by the produced deuterons (here in the inner and denser part of the cloud; $<$100 au) also happens when such particles are implanted in matter (grains) or have low enough energy to be captured and produce molecules such as HD or H_2D+. Therefore, these mechanisms could help to explain the enhancement of the D/H ratio in the inner regions of the MC (e.g., Tielens 1992). This fact is observed by radio observation of molecules in nearby MCs (e.g., Punanova et al. 2016) and also described by astrochemical models of such regions (e.g., Roberts et al. 2004; Amin & Kordi 2009).

Figure 9 shows the energy deposition for pion+, pion−, muon+, and muon− inside the MC. For all of these secondary particles, one can observe a hard core in the central region of the MC, but it presents a very small delivered energy ($\sim 3 \times 10^{-12}$ MeV g^{-1} s^{-1} for pions and $\sim 2.4 \times 10^{-11}$ MeV g^{-1} s^{-1} for muons) compared to the other components. Simulations with pion0 were performed, but no energy deposition has been recorded for this particle. Therefore, the current work has found that the energy input of pions as a result of the cascading process triggered by primary CRs (protons and alphas) is negligible in most of the cloud, with the exception of its very deep core.

Tables A1–A4 (in the Appendix) present the obtained values for the deposited energy due to secondary particles, in units of MeV g^{-1} s^{-1}, in each shell layer of the simulated MC, employing the GEANT4 code. Table A1 presents the values for particles produced by a proton source only, Table A2 presents the values for particles produced by an alpha source only, Table A3 presents the values for particles produced by an electron source only, and Table A4 presents the summed values from the proton, alpha, and electron sources (realistic astrophysical scenario). The calculation error was below 10%. The data for pion− and muon− can also be found in the Appendix.

The total energy deposited by all of the CR-induced particles due to the primary protons, alphas, and electrons in the MC as a function of distance from the center is shown in Figure 10. The rightmost part of the figure presents the color map of the energy delivery by the secondary particles due to different input sources as a function of radius in au (the numbers in the radial axis are in logarithmic scale). A scale with the dimensions of the structures of the solar system is shown at the bottom of the figure. Three interesting points can be highlighted in this figure. (1) One observes that the energy deposited by all secondary particles due to the primary protons is much more relevant (about two to three times more). (2) The energy deposition by all secondary particles from primary alphas and electrons seems not to vary too much as a function of radius of the cloud ($\sim$50 MeV g^{-1} s^{-1}), presenting only a significant decrease in the central part. (3) The energy deposition by all secondary particles from primary protons presents a slight decrease toward the central parts and a soft bump around 450–3000 au reaching 210 MeV g^{-1} s^{-1}.

The calculated increase of the deposited energy in regions between the equivalent distances of the Kuiper Belt and the Oort cloud could be the origin of a pressure gradient responsible for the observed depletion of matter in that region. Future models will focus the energy delivered in the inner part of the cloud ($<$100 au) with higher spatial resolution to get a better description of the gradient of the delivered energy in deep regions close to the center. A model with energy deposition by CRs in the same MC geometry employing a primary spectrum modulated by a solar potential is presented for comparison purposes in Section 3.3. This comparison has shown that low-energy particles from the ISM indeed play an important role in the energy delivery within MCs.

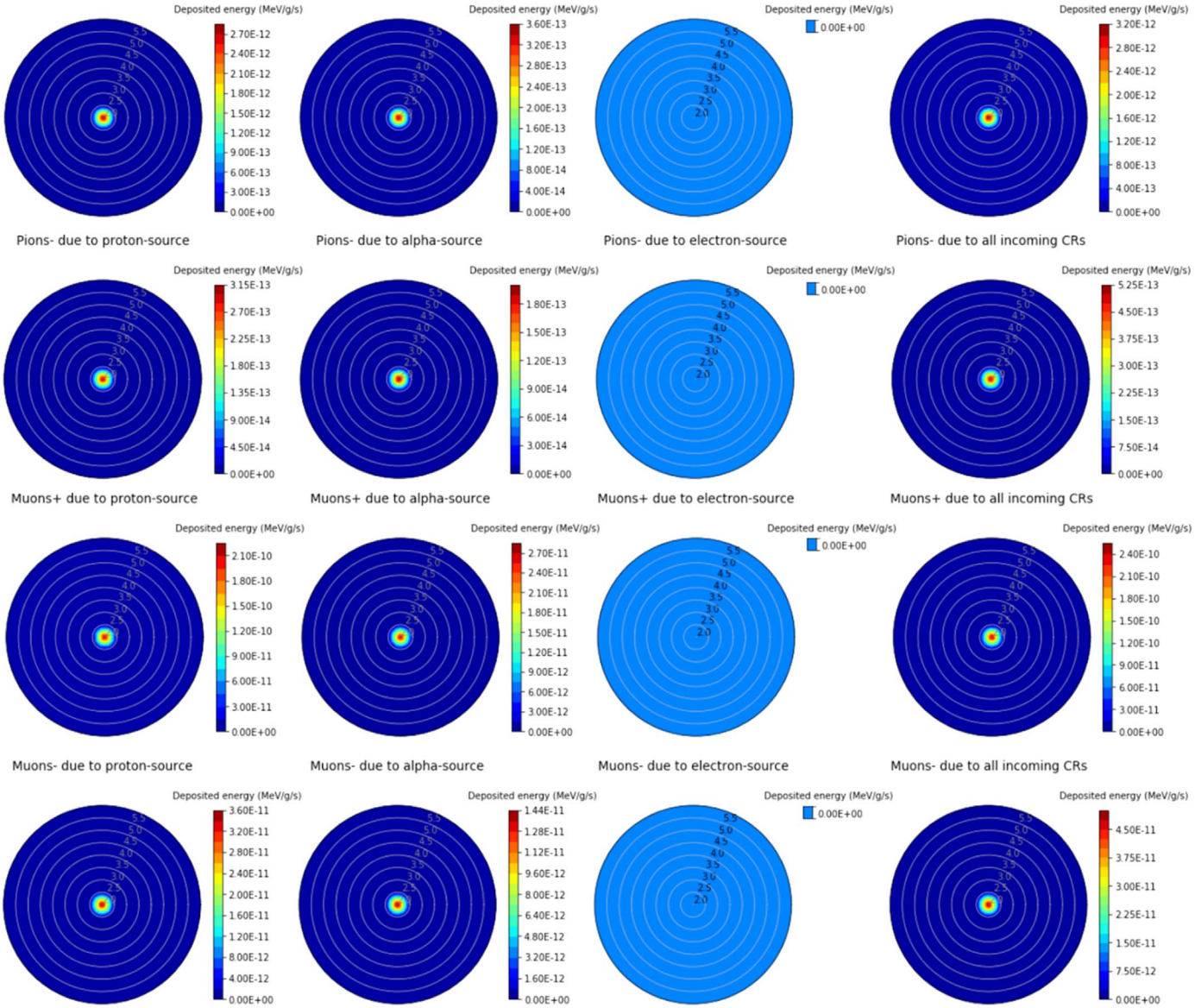

Figure 9. Color map of the energy delivery by pions+/− and muons+/− due to incoming CRs inside the MC. The rightmost panels present the summed values (considering proton, alpha, and electron CRs). The numbers in the radial axis are the sizes of a given outer layer in astronomical units (logarithmic scale).

Figure 11 presents the energy deposited by CR-induced particles as a function of distance within the MC. The numbers of the model layers are indicated. Panel (a) presents the values in units of MeV g^{-1} s^{-1}, and panel (b) presents them in percentage. We observe in both panels that the protons are the main agents of the energy delivery inside the MC, and the electrons are the second most important component. In Figure 11(a), we also observe that the components that are not protons, electrons, and alphas do not deposit significant energy in the MC. However, one can note that their energy delivery increases by at least 1 order of magnitude in the central region compared to the outer one. This effect can be explained due to the increasing density of the medium. The photon presents an increase of 1 order of magnitude against 2 and 5 orders of magnitude for the deuteron and muon, respectively. Particles such as pions and muons present a large enhancement in energy delivered in the central region, but the net value is very small ($\sim 1 \times 10^{-10}$ MeV g^{-1} s^{-1}) when compared with other particles. Neutrons do not deposit energy within this model.

Figure 11(b) presents the main contribution of secondary particles to the energy delivered within the protostellar core in percentage. We observe that in the central region, protons deposit ∼63%, electrons ∼30%, and alphas ∼4%; other components sum an energy delivered of about 3%. Primary and secondary electrons represent the other important input of energy in the MC (from 30% to 40% of the energy input). In the current model, we observe that in the deep core, the contribution of positrons in energy delivery can reach 40%. The amount of energy deposited by secondary alphas is very low in the deep core and increases toward the outer radius of the protostellar core, reaching ∼15% in the external border. The secondary deuterons and positrons together contribute around 1% of the energy input, mainly in the central regions up to 100 au.

3.2. Cloud Temperature Estimation

As pointed out by Pan & Padoan (2009, and references therein), the observed temperatures of the MCs are in the range between 7

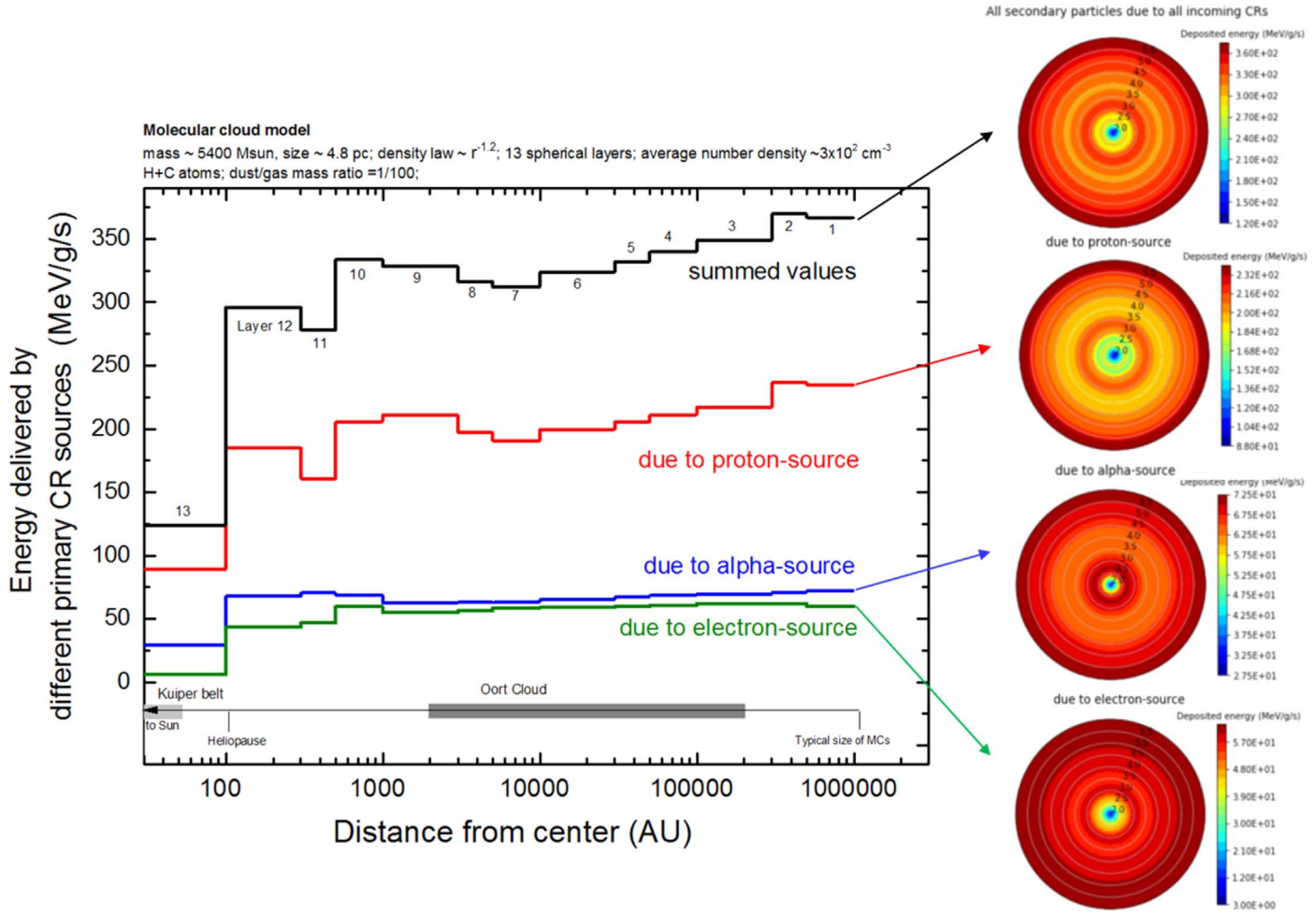

Figure 10. Energy delivery by primary cosmic radiation in the simulated MC considering the CR flux data from Voyager I measured at the ISM (Cummings et al. 2016). Model parameters are indicated in the figure header. A ruler with the dimensions of the solar system is presented for comparison purposes. Inset figures on the right present a color map with the energy deposition profile along the cloud (polar plot): energies deposited by total particles produced by the electron source (bottom), the alpha source (second from bottom), the proton source (second from top), and all sources (top). In the color map, red means higher energy deposition, and blue is the lowest energy deposition. The numbers in the radial axis are the sizes of a given outer layer in units of astronomical units (logarithmic scale). See details in the text.

and 15 K, and the typical lifetimes are in the range from roughly 10^5 yr to a few tens of megayears (e.g., Dobbs et al. 2014; Chevance et al. 2020). Here, in an attempt to calculate the temperature profile of the cloud (mainly the gas temperature ($T_{\rm gas}$) in the presence of incoming CRs) in a steady-state scenario, we consider the thermal balance of the gas and dust, coupled together by the gas–dust collisions. This is done by solving the thermal equilibrium condition (Goldsmith 2001),

$$G_{\rm gas,cr} - \Lambda_{\rm gas} - \Lambda_{\rm gd} = 0, \tag{2}$$

in which $G_{\rm gas,cr}$ is the energy delivered by CRs in each layer of the current model (a function of the local number density of molecular hydrogen, $n(\rm H_2)$, in units of erg cm^{-3} s^{-1}). In Equation (2) $\Lambda_{\rm gas}$ is the canonical gas cooling rate given by the expression

$$\Lambda_{\rm gas} = \alpha(T_{\rm gas}/10\ {\rm K})^{\beta}\ ({\rm erg\ cm^{-3}\ s^{-1}}) \tag{3}$$

with and depending on the $\rm H_2$ number density (see Goldsmith 2001), and $\Lambda_{\rm gd}$ is the gas–dust energy transfer rate per unit volume (e.g., Burke & Hollenbach 1983; Goldsmith 2001), given by the expression

$$\Lambda_{\rm gd} = 2 \times 10^{-33}(n({\rm H_2})/{\rm cm^{-3}})^2 \times ((T_{\rm gas} - T_{\rm dust})/{\rm K}) \times (T_{\rm gas}/10\ {\rm K})^{0.5}\ ({\rm erg\ cm^{-3}\ s^{-1}}), \tag{4}$$

with the temperature of dust inside the cloud ($T_{\rm dust}$) ranging from 6–8 K depending on the $n(\rm H_2)$, which also considers a typical gas–dust coupling and an intermediate molecular depletion, as discussed in the DF model from Goldsmith (2001). The considered values in the calculation of gas temperature (cloud temperature) are listed in Table 2.

A detailed discussion of the employed equations and approximations considered is shown in Goldsmith (2001, and references therein). However, it is worth noting that, as discussed by Goldsmith (2001), when gas–dust coupling is considered, the gas and dust temperatures calculated in the heat balance models of MCs are roughly the same ($T \sim 8$ K) at the very dense and central regions ($n(\rm H_2) > 10^6\ cm^{-3}$). Following the author, at the outer regions of the cloud, when densities are low ($n(\rm H_2) < 10^3\ cm^{-3}$), the gas temperature is expected to be a little higher ($T_{\rm gas} \sim$ 10–13 K) than the grain temperature ($T_{\rm dust} \sim 6$ K), considering or not considering the gas–grain

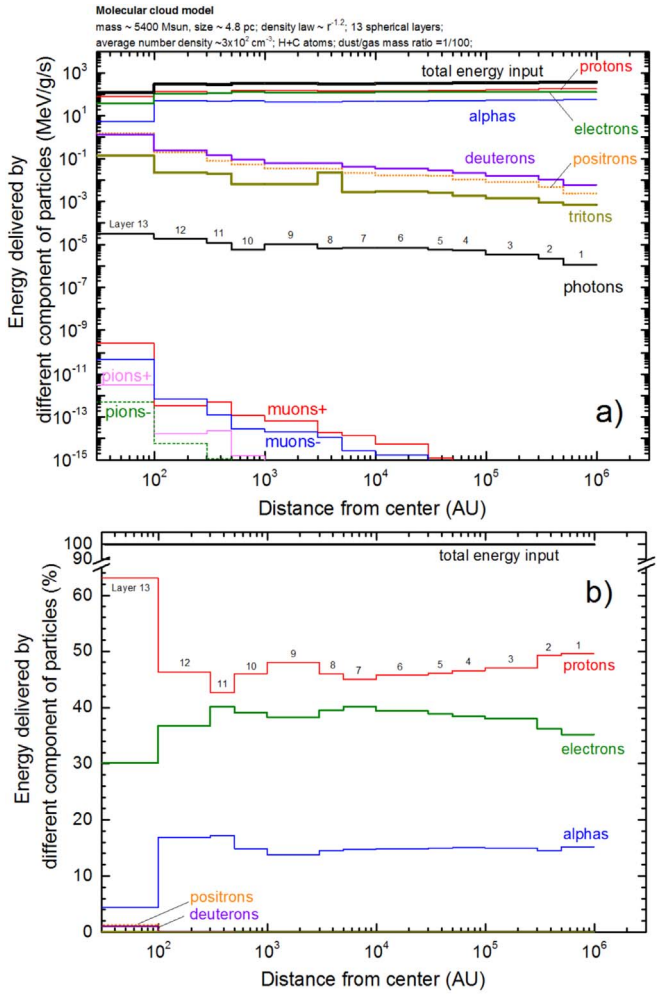

Figure 11. Energy delivery by different components of cosmic radiation (primary and secondary particles) in the simulated MC considering the CR flux data from Voyager I measured at the ISM. Model parameters are indicated in the figure header. Panel (a) is in units of MeV g^{-1} s^{-1}, and panel (b) is in percentage.

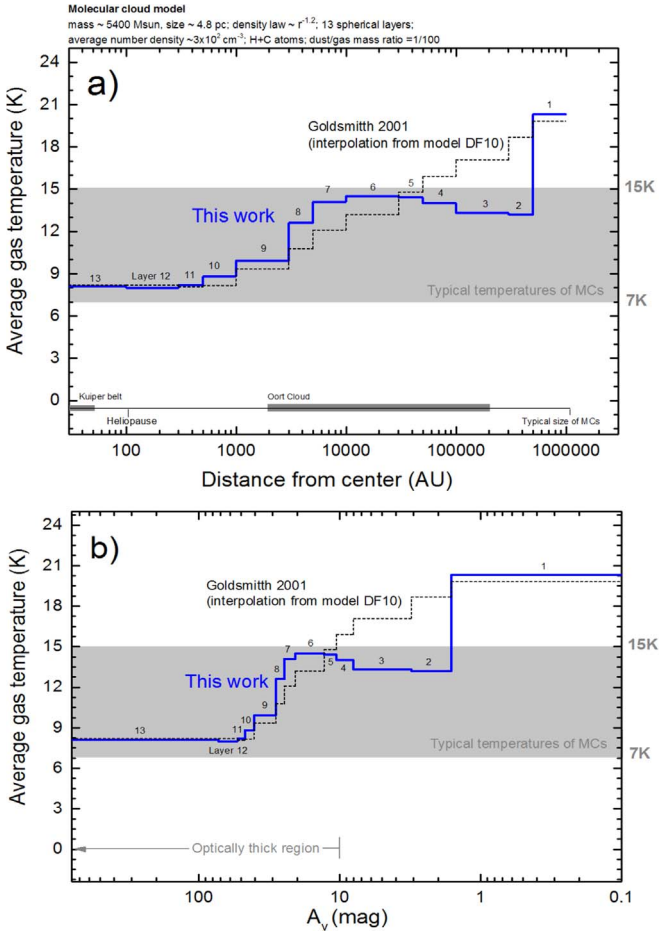

Figure 12. Average gas temperature (or cloud temperature profile) of each layer of the modeled MC exposed to CRs and considering the balance heat (Equation (2)). The blue line is the estimation employing current CR energy delivery, and the dashed black line is an interpolation from model DF10 of Goldsmith (2001). Panel (a) shows temperature as a function of distance from the center in au. For comparison purposes, a ruler with some dimensions inside the solar system is presented at the bottom of the figure. Panel (b) shows the temperature as a function of the average visual extinction of the layer as seen from outside of the cloud (see also in Figure 1). In both panels, the horizontal gray region indicates the typical temperature range of the MCs (7–15 K). The numbers of the layers in the model are indicated by the black labels.

coupling mechanisms. Following the author, the gas–grain coupling significantly reduces the gas temperatures at higher densities while only slightly raising the dust temperature. As discussed above, in our first-order model for temperature enhancement, we consider the same temperature for both atoms in a given layer; this implies in some way a gas–grain coupling.

Figure 12 presents the average gas temperature (or cloud temperature profile) of each layer of the modeled MC exposed to CRs and considering the balance heat of Equation (2). Panels (a) and (b) show temperature as a function of distance from the center in au and average visual extinction, respectively. The blue line is the estimation employing current CR energy delivery, and the dashed black line is an interpolation from model DF10 of Goldsmith (2001). We observe a great similarity between the two models, both showing gas temperature around 8 K in the center of the cloud and about 20 K at the outer edge. The major discrepancy (roughly 4 K) of those models was observed at a distance of around 1×10^5–5×10^5 au from the center (layers 3 and 2), in which our model shows lower values for temperature in comparison with the model of Goldsmith (2001). In contrast to Goldsmith's model, we observe a small bump in temperature at a distance of 3×10^3–2×10^4 au from the center. The current model also shows a rapid temperature decrease (roughly 7 K) between layers 1 and 2 (in the lower-density regions of the cloud that have the larger calculated CR energy delivered). Both models indicated that below the distance of 5×10^4 au ($Av > 10$), the gas temperature of the MC is below 15 K.

The enhancement of temperature induced by CRs in the different layers of the MC also affects its chemical balance, since it allows some reaction routes to occur in a more efficient way. The energy delivered and the heating due to specific secondary particles, including induced different ionizing photons, as well as its influence in chemical reaction within the cloud, will be a subject of future work with implications in the astrochemistry and astrobiology fields.

The study of the direct bombardment effects triggered by CRs in astrophysical ices (or grains) and their influence on the chemical composition of the targets has been performed experimentally (e.g., de Barros et al. 2011; Andrade et al. 2013; Portugal et al. 2014). As expected, the authors found, for instance, that for projectiles with high energies, the transferred energy occurs by Coulomb interaction with the target electrons (being characterized by the electronic stopping power, Se),

Table 2
Parameters Employed in the Calculation of T_{gas} (or Cloud Temperature) from Heating Induced by CRs in the MC Model Described by This Work

Layer	Deposited CR Energy, $G_{gas,cr}$ (MeV g^{-1} s^{-1})	Deposited CR Energy, $G_{gas,cr}$ (erg cm^{-3} s^{-1})	Average Layer Density, ρ (g cm^{-3})	Average $n(H_2)$ (cm^{-3})	Average Log ($n(H_2)$)	α[a] (erg cm^{-3} s^{-1})	β[a]	T_{dust}[b] (K)	T_{gas}[c] (K)
1	366.86	3.82E−25	6.50E−22	196.27	2.3	1.2E−25	1.7	6.0	20.3
2	369.71	8.84E−25	1.49E−21	450.90	2.7	5.1E−25	2.0	6.1	13.2
3	348.86	2.71E−24	4.85E−21	1463.01	3.2	1.4E−24	2.3	6.2	13.3
4	339.82	5.60E−24	1.03E−20	3110.65	3.5	2.3E−24	2.5	6.3	14.0
5	332.27	1.26E−23	2.37E−20	7146.33	3.9	4.4E−24	2.7	6.6	14.4
6	323.73	3.98E−23	7.68E−20	23187.14	4.4	1.1E−23	2.9	7.0	14.5
7	311.88	8.15E−23	1.63E−19	49299.49	4.7	1.6E−23	3.0	7.4	14.1
8	316.42	1.90E−22	3.75E−19	113261.31	5.1	2.3E−23	3.1	7.5	12.6
9	328.32	6.40E−22	1.28E−18	367477.39	5.6	3.8E−23	3.2	7.6	9.9
10	334.08	1.38E−21	2.59E−18	781356.78	5.9	4.6E−23	3.3	7.6	8.8
11	278.14	2.65E−21	5.95E−18	1.79509E6	6.3	5.5E−23	3.4	7.7	8.2
12	296.16	9.14E−21	1.93E−17	5.82422E6	6.7	6.8E−23	3.7	7.8	8.0
13	123.89	1.13E−18	5.69E−15	1.71696E9	9.2	1.2E−22	4.7	8.0	8.1

Notes.
[a] Interpolated values considering the gas cooling function described by Goldsmith (2001).
[b] Interpolated values considering typical gas–dust coupling and intermediate molecular depletion (from model DF10 of Goldsmith 2001).
[c] Calculated in this work by considering the balance heating described in Equation (2).

whereas low-energy projectiles transfer their energy mainly through elastic collisions with the atomic nuclei of target atoms (being characterized in this case by the so-called nuclear stopping power, Sn). The effective molecular destruction cross section (σ_d) by ion projectile follows a power law as a function of the electronic stopping power. According de Barros et al. (2011), σ_d is proportional to $Se^{1.5}$, suggesting that grain processing is ruled out not only by its initial chemical composition and temperature but also by the stopping power of the incoming projectile (and not explicitly by the type of the incoming projectile) and, additionally, the ion flux (ϕ). Moreover, Andrade et al. (2013) showed that for the calculation of the effective molecular dissociation rates in ices ($k_d = \sigma_d \times \phi$) triggered by ions with high energies (>10 MeV nucleon^{-1}), Fe is an important component despite its very low abundance in comparison with the most abundant ones (protons and alphas). In the present work, we focus on the interactions between CRs with atoms/molecules in the gas phase (grains represent only about 1% of total mass), the energy deposition within the cloud, and its eventual heating triggered by CRs. The calculation of an effective molecular dissociation cross section or molecular dissociation rates is outside the scope of this paper. Future works may investigate the influence of the low abundant Fe ions of the CR inventory in the projectile cascade within the MCs and help to clarify these issues.

3.3. Model Employing Primary Cosmic Radiation with Solar Potential (CR Flux at 1 au)

Considering that the Voyager I spectrum measurements are recent and the CR spectra at 1 au are often used, simulations have been performed with the spectra modulated by the solar potential for comparison purposes. The primary cosmic radiation here was based on the work of Mathiä et al. (2013) and considered CRs measured at 1 au. The main differences between the two employed CR fluxes are in the low-energy part of the spectrum (<1 GeV) of incoming projectiles, as well as the presence of electrons. Here we considered that primary cosmic radiation is composed of only protons and alphas and represents about 98% of the total galactic cosmic radiation field (Dorman 2004). The model generates the cosmic radiation that arrives at the top of the magnetosphere subject to the solar potential. In order to minimize the solar activity influence on the primary spectra, we considered the minimum solar heliocentric potential corresponding to 234 MV (2009 December) without cutoff rigidity. Therefore, the primary fluence rates that we have obtained for simulations are 2.49 protons and 0.23 alphas cm^{-2} s^{-1}, with mean energies of 2.52 and 7.01 GeV, respectively.

Figure 13 shows the proton and alpha energy spectra employed in this model compared with spectra measured by Voyager I in the ISM and employed in the model described in Section 3.1. For both protons and alphas, we can notice a divergence between the spectra at the ISM and 1 au. This divergence starts to be relevant for energies lower than ~1 GeV and is due to the solar potential modulation at 1 au. As a consequence, the average energy of the primary particles considering the solar potential is higher than that measured at Voyage I. The model at 1 au neglects the electron flux.

The total energy delivered by primary protons and alphas considering the CR flux measured at 1 au (from Mathiä et al. 2013) in the MC is shown in Figure 14. Three interesting points can be highlighted in this figure. (i) The energy deposited by all

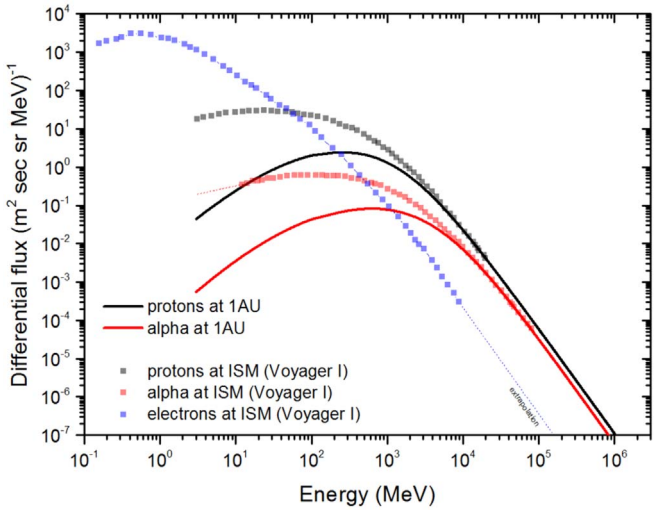

Figure 13. Comparison between primary CR energy spectra in the ISM obtained by Voyager I (Cummings et al. 2016), employed in the previous sections, and the values determined at earth orbit (1 au) modulated by solar potential, not considering the low-energy protons and alpha particles, as well as the electron component (Mathiä et al. 2013). See details in the text.

secondary particles due to the primary protons is also the dominant component, as we also observed when CR flux from the ISM was employed (see also Figure 10). (ii) The energy deposition by all secondary particles from primary alphas seems not to vary too much as a function of the radius of the cloud (~13.5 MeV g^{-1} s^{-1}), presenting only a slight decrease in the central part. This behavior is also similar to the model employing Voyager I data. However, in the case of Voyager I CR flux, the energy deposited is higher (~50 MeV g^{-1} s^{-1}) and presents a more significant decrease in the center region. (iii) The energy deposition by all secondary particles from primary protons presents a slight increase toward the central parts and a strong bump around 400 au reaching 39.2 MeV g^{-1} s^{-1} against 210 MeV g^{-1} s^{-1} found using the Voyager spectrum.

Therefore, the comparison between the two MC models (one employing data from Voyager I in the ISM and the other employing data at 1 au) shows that the energy deposited considering the Voyager I spectrum is much higher than the employment data at 1 au, and here we can notice a prominent energy bump at 400 au. Moreover, we also observe that when CRs modulated by the solar potential are considered, the energy deposited in the center of the cloud is higher than the deposited values in the outer layers. When a CR flux with low-energy particles is considered (as in the case of the Voyager I data), we observe the opposite behavior; the outer part of the clouds receives more energy than the inner core, indicating that lower-energy particles deposit lots of their energy in the outer layers of the MC (even in regions with low densities).

4. Conclusion

Simulations of the energy released by CR-induced particles in a typical MC (mass 5400 $M_\odot$ containing H (major) and C atoms, size ~4.8 pc, density law $r^{-1.2}$, average number density ~300 cm^{-3}) were carried out by employing the Monte Carlo code GEANT4, which takes into account nuclear physics and cascade particle processes. In the main simulation, we considered a CR flux measured by the Voyager spacecraft at the ISM (taken from Cummings et al. 2016). A second simulation employing CR flux modulated by the solar potential

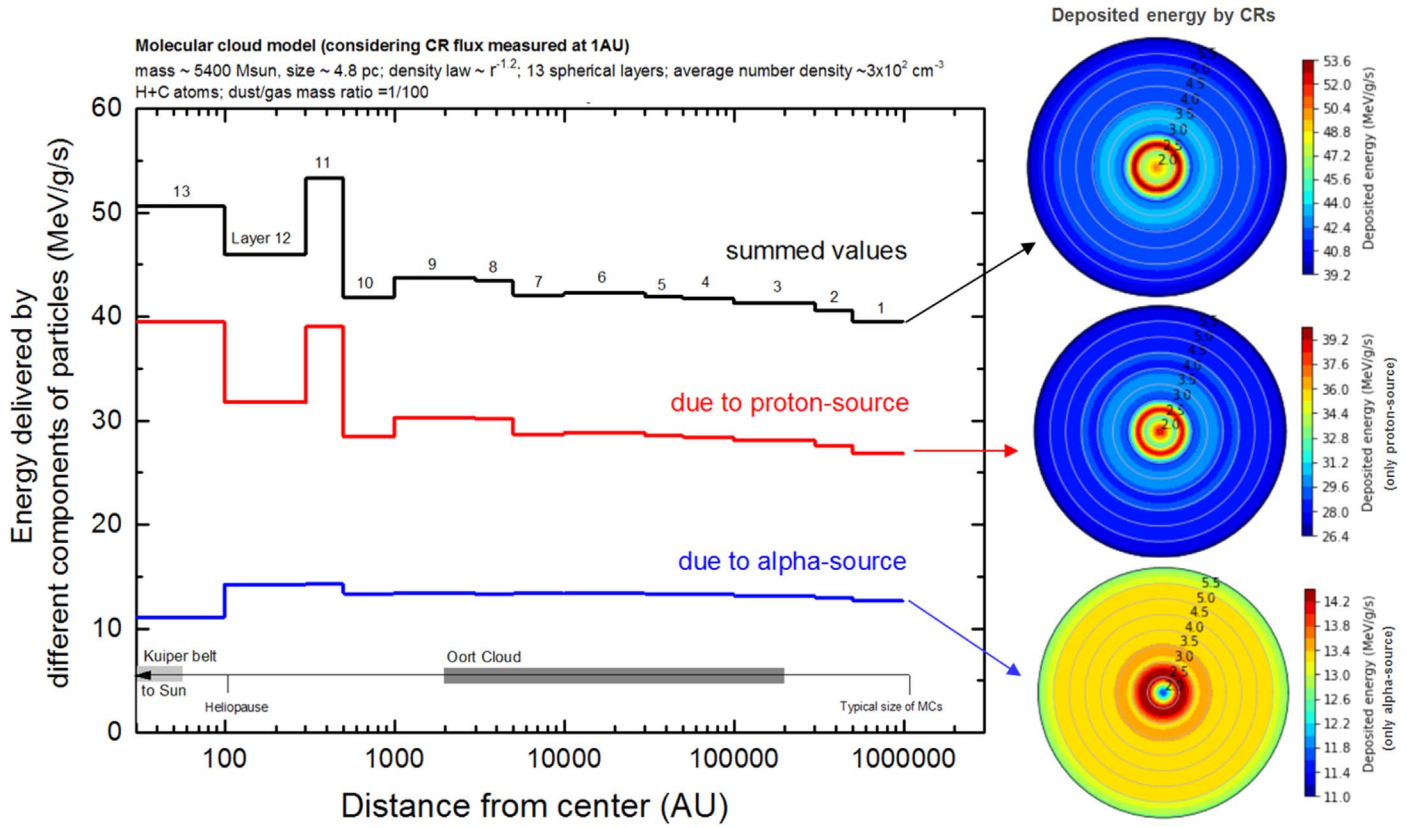

Figure 14. Total energy delivered by primary protons and alphas considering a CR flux measured at 1 au and modulated by the solar potential (from Mathiä et al. 2013). Only protons and alphas from 1 to 10^6 MeV were considered. Model parameters are indicated in the figure header. Inset figures on the right present a color map with the energy deposition profile along the cloud (polar plot): energies deposited by the total particles produced by the alpha source (bottom), the proton source (middle), and all sources (top). See also Figure 10 for comparison purposes.

(taken from Mathiä et al. 2013) was also performed for comparison purposes. We have determined the energy deposition rate of several kinds of particles (proton, alpha, electron, photon, electron, positron, pion+, pion−, muon+, muon−, deuteron, and triton) as a function of the CR's primary source type and the distance to the center of the MC. The energy deposited allows us to estimate the temperature gradient between the MC volumes by using a first-order approximation. The main conclusions are as follows.

(1) Protons are the main agents of the energy delivery and heating process inside the MC. The dose from protons is the most important component of the dose rate deposited in all regions of the MC. This component delivers up to $\sim$230 MeV g^{-1} s^{-1} in the outer region.
(2) Electrons due to the proton, alpha, and electron sources are the second most important component for energy deposition in almost all layers of the MC. The secondary electrons can deliver an energy rate of $\sim$130 MeV g^{-1} s^{-1} in the outer region of the MC. However, electrons deposit an energy rate of about 35.0 MeV g^{-1} s^{-1} in the center region (up to 100 au).
(3) Secondary alphas due to the proton source deliver more energy in a ring region between $\sim 1 \times 10^3$ and 3×10^4 au. The energy deposited presents values up to $\sim 1.40 \times 10^{-2}$ MeV g^{-1} s^{-1} and decreases significantly in the center region.
(4) The total energy deposited rate by all secondary particles shows an almost constant behavior for outer regions and a cold region in the central part (100 au). The energy delivered is $\sim$320 MeV g^{-1} s^{-1} for the outer regions and $\sim$125 MeV g^{-1} s^{-1} in the central part.
(5) Muons, pions, deuterons and tritons present a much lower energy deposition rate compared to protons, alphas, and electrons. All of these components present a hard core located in the central region of the MC for proton and alpha primary particles. Neutrons and muon0 do not deposit energy in all MCs, mainly due to their decay process time.
(6) The implantation of deuterons (results from the cascade of reactions from incoming protons and alpha sources) in the inner and denser parts of clouds (<100 au) enriches the D/H regions in this region. This might indicate that molecules formed in the inner parts of clouds have a D/H higher than molecules formed in the outer parts of clouds (less dense regions).
(7) From the temperature model (considering CR data from Voyager I), the main conclusions were as follows. (i) A small bump in temperature at the distance of 3×10^3–2×10^4 au from the center is observed. (ii) It shows a rapid temperature decrease (roughly 7 K) between layers 1 and 2. (iii) Below the distance of 5×10^4 au ($Av > 10$), the gas temperature of the MC is below 15 K, in good agreement with previous models (see Goldsmith 2001).

The description of the profile of the energy deposition due to the different particles produced within the particle shower induced by primary CR bombardment on matter in the interstellar cloud helps us to identify regions where specific ionizing agents could trigger specific chemical reaction routes,

inducing some specificity in the molecular formation/destruction. Combining this information with the molecular maps from radio observations adds another piece to the puzzle of the chemistry network of MCs and reinforces the role of CRs in such environments.

M.T.P. thanks the São Paulo Research Foundation for the financial support (project 2019/13577-0). The work of J.M.Q. has been partially financed by the research project RTI2018-098117-B-C21 of the Spanish Ministerio de Ciencia, Innovación y Universidades. S.P. also acknowledges the Brazilian research agency CNPq (project Nos. 306145/2015-4 and 302985/2018-2).

Appendix
Energy Deposited in the MC Layers by Different Components of CRs

Tables A1–A4 present the obtained values for the deposited energy due to secondary particles, in units of MeV g^{-1} s^{-1}, in each shell layer of the simulated MC, employing the GEANT4 code.

Table A1

Energy Deposited by Secondary Particles Due to the Proton Source (Incoming Primary Proton CR Component) in Each Shell Layer in Units of MeV g^{-1} s^{-1}

Layer No.	Outer and Inner Shell Radii (au)	Proton	Alpha	Electron	Positron	Photon (gamma)	Neutron	Deuteron	Triton	Pion+	Pion−	Pion0	Muon+	Muon−
1	9.4E+05–5.0E+05	1.82E+02	9.20E−03	5.27E+01	2.18E−03	1.91E−07	0.00E+00	1.31E−03	2.46E−04	5.73E−19	1.71E−19	0.00E+00	4.22E−17	1.54E−17
2	5.0E+05–3.0E+05	1.82E+02	1.20E−02	5.46E+01	4.30E−03	3.90E−07	0.00E+00	1.57E−03	4.00E−05	1.30E−18	4.13E−19	0.00E+00	1.24E−16	4.67E−17
3	3.0E+05–1.0E+05	1.64E+02	1.07E−02	5.32E+01	7.31E−03	5.46E−07	0.00E+00	1.83E−03	6.45E−05	3.72E−18	8.91E−19	0.00E+00	3.37E−16	9.66E−17
4	1.0E+05–5.0E+04	1.58E+02	9.55E−03	5.30E+01	9.68E−03	9.44E−07	0.00E+00	2.30E−03	1.18E−04	6.12E−18	2.34E−18	0.00E+00	6.48E−16	2.42E−16
5	5.0E+04–3.0E+04	1.53E+02	9.16E−03	5.25E+01	1.45E−02	1.20E−06	0.00E+00	3.00E−03	2.74E−04	1.15E−17	4.85E−18	0.00E+00	1.05E−15	4.00E−16
6	3.0E+04–1.0E+04	1.48E+02	1.41E−02	5.16E+01	1.47E−02	1.56E−06	0.00E+00	2.43E−03	2.35E−04	5.31E−17	1.01E−17	0.00E+00	4.65E−15	1.10E−15
7	1.0E+04–5.0E+03	1.40E+02	1.45E−02	5.05E+01	1.95E−02	8.04E−07	0.00E+00	2.18E−03	7.36E−04	1.69E−16	2.28E−17	0.00E+00	1.30E−14	2.15E−15
8	5000–3000	1.45E+02	1.12E−02	5.21E+01	3.11E−02	1.24E−06	0.00E+00	2.44E−03	6.08E−04	1.76E−16	8.96E−17	0.00E+00	1.74E−14	9.76E−15
9	3000–1000	1.57E+02	1.04E−02	5.40E+01	3.09E−02	1.50E−06	0.00E+00	3.59E−03	7.39E−04	4.86E−16	2.22E−16	0.00E+00	6.08E−14	1.71E−14
10	1000–500	1.53E+02	0.00E+00	5.26E+01	4.71E−02	3.17E−07	0.00E+00	0.00E+00	0.00E+00	1.41E−15	8.58E−17	0.00E+00	1.04E−13	7.63E−15
11	500–300	1.18E+02	0.00E+00	4.27E+01	7.06E−02	4.41E−06	0.00E+00	0.00E+00	0.00E+00	2.29E−14	5.19E−16	0.00E+00	4.75E−13	8.37E−14
12	300–100	1.36E+02	0.00E+00	4.90E+01	1.79E−01	4.43E−06	0.00E+00	0.00E+00	0.00E+00	1.61E−14	5.64E−15	0.00E+00	3.00E−13	6.88E−13
13	100–0	7.27E+01	0.00E+00	1.48E+01	1.37E+00	6.64E−06	0.00E+00	1.34E−02	0.00E+00	2.80E−12	3.06E−13	0.00E+00	2.19E−10	3.53E−11
Sum	9.4E+05–0	1.91E+03	1.01E−01	6.33E+02	1.80E+00	2.42E−05	0.00E+00	3.40E−02	3.06E−03	2.84E−12	3.13E−13	0.00E+00	2.19E−10	3.61E−11

Note. The calculation error was below 10%.

Table A2
Energy Deposited by Secondary Particles Due to the Alpha Source (Incoming Primary Alpha CR Component) in Each Shell Layer in Units of MeV g^{-1} s^{-1}

Layer No.	Outer and Inner Shell Radii (au)	Proton	Alpha	Electron	Positron	Photon (gamma)	Neutron	Deuteron	Triton	Pion+	Pion−	Pion0	Muon+	Muon−
1	9.4E+05–5.0E+05	4.64E−02	5.57E+01	1.64E+01	2.42E−04	6.35E−08	0.00E+00	4.68E−03	4.53E−04	5.92E−20	4.04E−20	0.00E+00	5.76E−18	3.30E−18
2	5.0E+05–3.0E+05	8.38E−02	5.38E+01	1.71E+01	4.72E−04	1.18E−07	0.00E+00	8.90E−03	8.53E−04	1.24E−19	9.87E−20	0.00E+00	1.05E−17	9.27E−18
3	3.0E+05–1.0E+05	1.28E−01	5.22E+01	1.73E+01	7.64E−04	1.77E−07	0.00E+00	1.42E−02	1.35E−03	4.23E−19	2.34E−19	0.00E+00	3.77E−17	2.02E−17
4	1.0E+05–5.0E+04	1.74E−01	5.10E+01	1.72E+01	1.13E−03	2.47E−07	0.00E+00	1.94E−02	1.76E−03	7.29E−19	2.77E−19	0.00E+00	4.89E−17	3.20E−17
5	5.0E+04–3.0E+04	2.14E−01	4.97E+01	1.71E+01	1.52E−03	2.78E−07	0.00E+00	2.55E−02	2.39E−03	2.40E−18	6.25E−19	0.00E+00	1.76E−16	6.99E−17
6	3.0E+04–1.0E+04	2.60E−01	4.80E+01	1.68E+01	2.03E−03	3.40E−07	0.00E+00	3.32E−02	2.66E−03	4.33E−18	7.33E−18	0.00E+00	1.04E−15	6.14E−16
7	1.0E+04–5.0E+03	2.98E−01	4.61E+01	1.65E+01	2.04E−03	5.25E−07	0.00E+00	4.01E−02	2.02E−03	3.47E−17	8.74E−18	0.00E+00	7.65E−16	5.73E−16
8	5000–3000	3.91E−01	4.58E+01	1.68E+01	2.77E−03	5.25E−07	0.00E+00	5.86E−02	2.24E−02	2.12E−16	5.34E−17	0.00E+00	1.26E−15	1.52E−15
9	3000–1000	5.03E−01	4.51E+01	1.68E+01	4.00E−03	1.45E−06	0.00E+00	5.73E−02	5.92E−03	6.09E−17	5.25E−17	0.00E+00	5.53E−15	4.09E−15
10	1000–500	6.29E−01	4.97E+01	1.84E+01	5.70E−03	1.92E−07	0.00E+00	8.91E−02	6.31E−03	1.95E−16	1.66E−16	0.00E+00	1.58E−14	2.06E−14
11	500–300	6.02E−01	4.77E+01	2.20E+01	7.80E−03	7.33E−07	0.00E+00	1.41E−01	2.00E−02	4.72E−16	6.12E−16	0.00E+00	3.91E−14	4.41E−14
12	300–100	1.00E+00	4.99E+01	1.66E+01	1.98E−02	4.94E−07	0.00E+00	2.41E−01	2.27E−02	1.05E−15	2.42E−16	0.00E+00	3.75E−14	1.94E−14
13	100–0	5.45E+00	5.45E+00	1.66E+01	1.61E−01	1.66E−06	0.00E+00	1.32E+00	1.41E−01	3.55E−13	2.00E−13	0.00E+00	2.73E−11	1.43E−11
Sum	9.4E+05–0	9.78E+00	6.00E+02	2.26E+02	2.09E−01	6.80E−06	0.00E+00	2.05E+00	2.30E−01	3.57E−13	2.01E−13	0.00E+00	2.74E−11	1.44E−11

Note. The calculation error was below 10%.

Table A3

Energy Deposited by Secondary Particles Due to the Electron Source (Incoming Primary Electron CR Component) in Each Shell Layer in Units of MeV g^{-1} s^{-1}

Layer No.	Outer and Inner Shell Radii (au)	Proton	Alpha	Electron	Positron	Photon (gamma)	Neutron	Deuteron	Triton	Pion+	Pion−	Pion0	Muon+	Muon−
1	9.4E+05–5.0E+05	0.00E+00	0.00E+00	6.00E+01	2.35E−07	8.76E−07	0.00E+00	0.00E+00	0.00E+00	0.00E+00	0.00E+00	0.00E+00	0.00E+00	0.00E+00
2	5.0E+05–3.0E+05	0.00E+00	0.00E+00	6.21E+01	1.17E−06	1.71E−06	0.00E+00	0.00E+00	0.00E+00	0.00E+00	0.00E+00	0.00E+00	0.00E+00	0.00E+00
3	3.0E+05–1.0E+05	0.00E+00	0.00E+00	6.20E+01	1.17E−06	2.59E−06	0.00E+00	0.00E+00	0.00E+00	0.00E+00	0.00E+00	0.00E+00	0.00E+00	0.00E+00
4	1.0E+05–5.0E+04	0.00E+00	0.00E+00	6.04E+01	7.14E−07	4.05E−06	0.00E+00	0.00E+00	0.00E+00	0.00E+00	0.00E+00	0.00E+00	0.00E+00	0.00E+00
5	5.0E+04–3.0E+04	0.00E+00	0.00E+00	5.97E+01	2.18E−06	4.41E−06	0.00E+00	0.00E+00	0.00E+00	0.00E+00	0.00E+00	0.00E+00	0.00E+00	0.00E+00
6	3.0E+04–1.0E+04	0.00E+00	0.00E+00	5.90E+01	5.96E−06	4.97E−06	0.00E+00	0.00E+00	0.00E+00	0.00E+00	0.00E+00	0.00E+00	0.00E+00	0.00E+00
7	1.0E+04–5.0E+03	0.00E+00	0.00E+00	5.84E+01	2.16E−05	5.50E−06	0.00E+00	0.00E+00	0.00E+00	0.00E+00	0.00E+00	0.00E+00	0.00E+00	0.00E+00
8	5000–3000	0.00E+00	0.00E+00	5.62E+01	5.05E−05	4.74E−06	0.00E+00	0.00E+00	0.00E+00	0.00E+00	0.00E+00	0.00E+00	0.00E+00	0.00E+00
9	3000–1000	0.00E+00	0.00E+00	5.48E+01	0.00E+00	7.07E−06	0.00E+00	0.00E+00	0.00E+00	0.00E+00	0.00E+00	0.00E+00	0.00E+00	0.00E+00
10	1000–500	0.00E+00	0.00E+00	5.96E+01	0.00E+00	5.29E−06	0.00E+00	0.00E+00	0.00E+00	0.00E+00	0.00E+00	0.00E+00	0.00E+00	0.00E+00
11	500–300	0.00E+00	0.00E+00	4.69E+01	0.00E+00	6.44E−06	0.00E+00	0.00E+00	0.00E+00	0.00E+00	0.00E+00	0.00E+00	0.00E+00	0.00E+00
12	300–100	0.00E+00	0.00E+00	4.32E+01	0.00E+00	1.37E−05	0.00E+00	0.00E+00	0.00E+00	0.00E+00	0.00E+00	0.00E+00	0.00E+00	0.00E+00
13	100–0	0.00E+00	0.00E+00	5.88E+00	0.00E+00	2.23E−05	0.00E+00	0.00E+00	0.00E+00	0.00E+00	0.00E+00	0.00E+00	0.00E+00	0.00E+00
Sum	9.4E+05–0	0.00E+00	0.00E+00	6.88E+02	8.35E−05	8.36E−05	0.00E+00	0.00E+00	0.00E+00	0.00E+00	0.00E+00	0.00E+00	0.00E+00	0.00E+00

Note. The calculation error was below 10%.

Table A4

Total Energy Deposited by Secondary Particles (Summed Values from the Proton, Alpha, and Electron Sources, the Realistic Scenario) in Each Shell Layer in Units of MeV g^{-1} s^{-1}

Layer No.	Outer and Inner Shell Radii (au)	Proton	Alpha	Electron	Positron	Photon (gamma)	Neutron	Deuteron	Triton	Pion+	Pion−	Pion0	Muon+	Muon−
1	9.4E+05–5.0E+05	1.8205E+02	5.5709E+01	1.2910E+02	2.4222E−03	1.1305E−06	0.0000E+00	5.9900E−03	6.9900E−04	6.3220E−19	2.1140E−19	0.0000E+00	4.7960E−17	1.8700E−17
2	5.0E+05–3.0E+05	1.8208E+02	5.3812E+01	1.3380E+02	4.7732E−03	2.2180E−06	0.0000E+00	1.0470E−02	8.9300E−04	1.4240E−18	5.1170E−19	0.0000E+00	1.3450E−16	5.5970E−17
3	3.0E+05–1.0E+05	1.6413E+02	5.2211E+01	1.3250E+02	8.0752E−03	3.3130E−06	0.0000E+00	1.6030E−02	1.4145E−03	4.1430E−18	1.1250E−18	0.0000E+00	3.7470E−16	1.1680E−16
4	1.0E+05–5.0E+04	1.5817E+02	5.1010E+01	1.3060E+02	1.0811E−02	5.2410E−06	0.0000E+00	2.1700E−02	1.8780E−03	6.8490E−18	2.6170E−18	0.0000E+00	6.9690E−16	2.7400E−16
5	5.0E+04–3.0E+04	1.5321E+02	4.9709E+01	1.2930E+02	1.6022E−02	5.8880E−06	0.0000E+00	2.8500E−02	2.6640E−03	1.3900E−17	5.4750E−18	0.0000E+00	1.2260E−15	4.6990E−16
6	3.0E+04–1.0E+04	1.4826E+02	4.8014E+01	1.2740E+02	1.6736E−02	6.8700E−06	0.0000E+00	3.5630E−02	2.8950E−03	5.7430E−17	1.7430E−17	0.0000E+00	5.6900E−15	1.7140E−15
7	1.0E+04–5.0E+03	1.4030E+02	4.6115E+01	1.2540E+02	2.1562E−02	6.8290E−06	0.0000E+00	4.2280E−02	2.7560E−03	2.0370E−16	3.1540E−17	0.0000E+00	1.3765E−14	2.7230E−15
8	5000–3000	1.4539E+02	4.5811E+01	1.2510E+02	3.3921E−02	6.5050E−06	0.0000E+00	6.1040E−02	2.3008E−02	3.8800E−16	1.4300E−16	0.0000E+00	1.8660E−14	1.1280E−14
9	3000–1000	1.5750E+02	4.5110E+01	1.2560E+02	3.4900E−02	1.0020E−05	0.0000E+00	6.0890E−02	6.6590E−03	5.4690E−16	2.7450E−16	0.0000E+00	6.6330E−14	2.1190E−14
10	1000–500	1.5363E+02	4.9700E+01	1.3060E+02	5.2800E−02	5.7990E−06	0.0000E+00	8.9100E−02	6.3100E−03	1.6050E−15	2.5180E−16	0.0000E+00	1.1980E−13	2.8230E−14
11	500–300	1.1860E+02	4.7700E+01	1.1160E+02	7.8400E−02	1.1583E−05	0.0000E+00	1.4100E−01	2.0000E−02	2.3372E−14	1.1310E−15	0.0000E+00	5.1410E−13	1.2780E−13
12	300–100	1.3700E+02	4.9900E+01	1.0880E+02	1.9880E−01	1.8624E−05	0.0000E+00	2.4100E−01	2.2700E−02	1.7150E−14	5.8820E−15	0.0000E+00	3.3750E−13	7.0740E−13
13	100–0	7.8150E+01	5.4500E+00	3.7280E+01	1.5310E+00	3.0600E−05	0.0000E+00	1.3334E+00	1.4100E−01	3.1550E−12	5.0600E−13	0.0000E+00	2.4630E−10	4.9600E−11
Sum	9.4E+05–0	1.9185E+03	6.0025E+02	1.5471E+03	2.0102E+00	1.1462E−04	0.0000E+00	2.0870E+00	2.3288E−01	3.1983E−12	5.1374E−13	0.0000E+00	2.4738E−10	5.0501E−11

Note. The calculation error was below 10%.

ORCID iDs

Mauricio Tizziani Pazianotto https://orcid.org/0000-0001-8783-7089
Sergio Pilling https://orcid.org/0000-0002-6321-3666
Jose Manuel Quesada Molina https://orcid.org/0000-0002-2038-2814
Claudio Antonio Federico https://orcid.org/0000-0002-8263-0270

References

Agostinelli, S., Allisson, J., Amako, K., et al. 2003, NIMPA, 506, 250
Allison, J., Amako, K., Apostolakis, J., et al. 2006, ITNS, 53, 270
Amin, Y. M., & Kordi, A. S. 2009, J. King Saud Univ.—Sci., 21, 85
Andrade, D. P. P., de Barros, A. L. F., & Pilling, S. 2013, MNRAS, 430, 787
Boettcher, E., Zweibel, E. G., Yoast-Hull, T. M., & Gallagher, J. S., III 2013, ApJ, 779, 12
Bohlin, R. C., Savage, B. D., & Drake, J. F. 1978, ApJ, 224, 132
Brown, A., & Suit, H. 2004, Radiother. Oncol., 73, 265
Burke, J. R., & Hollenbach, D. J. 1983, ApJ, 265, 223
Chevance, M., Diederik Kruijssen, J. M., Hygate, A. P. S., et al. 2020, SSRv, 216, 50
Cui, Y., Puhlhofer, G., & Santangelo, A. 2016, A&A, 591, A68
Cummings, A. C., Stone, E. C., Heikkila, B. C., et al. 2016, ApJ, 831, 18
Dalgarno, A. 2006, PNAS, 103, 12269
Dalgarno, A., Yan, M., & Liu, W. 1999, ApJS, 125, 237
de Barros, A. L. F., Domaracka, A., Andrade, D. P. P., et al. 2011, MNRAS, 418, 1363
Dobbs, L. C., Krumholz, M. R., Ballesteros-Paredes, J., et al. 2014, in Protostars and Planets VI, ed. H. Beuther et al. (Tucson, AZ: Univ. Arizona Press), 3
Dorman, L. I. 2004, Cosmic Rays in the Earth's Atmosphere and Underground (Dordrecht: Kluwer Academic), 303
Draine, B. T. 2003, ARA&A, 41, 241
Filges, D., & Goldenbaum, F. 2010, Handbook of Spallation Research: Theory, Experiments and Applications (New York: Wiley)
Flynn, G. J., Nittler, L. R., & Engrand, C. 2016, Elements, 12, 177
Galli, D., & Padovani, M. 2015, in Proc. of Science 221, Cosmic Rays and the Interstellar Medium (CRISM 2014) (Trieste: SISSA), 019
Geant4 Collaboration 2012, GEANT4 Physics Reference Manual v9.6, https://geant4-userdoc.web.cern.ch/UsersGuides/PhysicsReferenceManual/BackupVersions/V9.6/fo/PhysicsReferenceManual.pdf
Glassgold, A. E., & Langer, W. D. 1973, ApJ, 186, 859
Goldsmith, P. F. 2001, ApJ, 557, 736
Goldsmith, P. F., & Langer, W. D. 1978, ApJ, 222, 881
Helling, C., Rimmer, P. B., Rodriguez-Barrera, I. M., et al. 2016, PPCF, 58, 074003
Herbst, E., & Cuppen, H. M. 2005, PNAS, 103, 12257
Jessberger, E. K., Stephan, T., Rost, D., et al. 2001, in Interplanetary Dust, ed. E. Grün et al. (Berlin: Springer), 253
Kataoka, R., & Sato, T. 2017, Geosci. Front., 8, 247
Krumholz, M. R. 2011, in AIP Conf. Proc. 1386, XV Special Courses at the National Observatory of Rio de Janeiro (AIP: Melville, NY), 9
Mathiä, D., Berger, T., Mrigakshi, A. I., & Reitz, G. 2013, AdSpR, 51, 329
Padovani, M., & Galli, D. 2013, Cosmic Rays in Star-Forming Environments (Berlin: Springer), 61
Padovani, M., Galli, D., & Glassgold, A. E. 2009, A&A, 501, 619
Pan, L., & Padoan, P. 2009, ApJ, 692, 594
Pelowitz, D. 2005, MCNPX User's Manual v2.5.0, LA-CP-05-0369, Los Alamos National Laboratory, https://rsicc.ornl.gov/codes/ccc/ccc8/ccc-810.html
Portugal, W., Pilling, S., Boduch, P., et al. 2014, MNRAS, 441, 3209
Punanova, A., Caselli, P., Pon, A., Belloche, A., & André, Ph. 2016, A&A, 587, A118
Roberts, H., Herbst, E., & Millar, T. J. 2004, A&A, 424, 905
Roman-Duval, J., Jackson, J. M., Heyer, M., Rathborne, J., & Simon, R. 2010, ApJ, 723, 492
Tielens, A. G. G. M. 1992, in IAU Symp. 150, Astrochemistry of Cosmic Phenomena, ed. P. D. Singh (Dordrecht: Kluwer Academic), 91
Tielens, A. G. G. M. 2005, The Physics and Chemistry of the Interstellar Medium (Cambridge: Cambridge Univ. Press)
Tielens, A. G. G. M., & Allamandola, L. J. 1987, in Interstellar Processes, ed. D. J. Hollenbach & H. A. Thronson (Dordrecht: Springer), 397
Toci, C., & Galli, D. 2015, MNRAS, 446, 2110
Tricco, T. S., Price, J. D., & Laibe, G. 2017, MNRAS, 471, L52
Vandenbroucke, B., & Wood, K. 2018, A&C, 23, 40
Vandenbroucke, B., Wood, K., Girichidis, P., Hill, A. S., & Peters, T. 2018, MNRAS, 476, 4032
Vaupre, S. 2015, PhD thesis, Université Grenoble Alpes, https://tel.archives-ouvertes.fr/tel-01273899/document
Wolfire, M. G., Hollenbach, D., & McKee, C. F. 2010, ApJ, 716, 1191
Wood, K., Mathis, J. S., & Ercolano, B. 2004, MNRAS, 348, 1337
Yeghikyan, A. G. 2011, ISRAA, 2011, 905015